

RESEARCH ARTICLE

Open Access



Biotic and environmental changes in the Panthalassa Ocean across the Norian (Late Triassic) impact event

Honami Sato^{1,2*} , Yutaro Takaya^{1,2,3,4}, Kazutaka Yasukawa^{1,4,5}, Koichiro Fujinaga^{1,4}, Tetsuji Onoue⁶ and Yasuhiro Kato^{1,2,4,5}

Abstract

Stratigraphic records of impact ejecta preserved in a pelagic deep-sea setting occur within Upper Triassic successions of the subduction-generated accretionary complexes of central Japan. A significant biotic turnover in radiolarians occurred during the ~ 300 kyr time interval after the impact event, which is characterized by a remarkable reduction in the burial flux of radiolarian silica. However, the nature of the environmental conditions at this time remains unclear. To investigate the environmental changes that triggered a decline in radiolarian burial flux after the impact event, geochemical proxies (major, trace, and rare earth elements) were applied to the middle–upper Norian (Upper Triassic) bedded chert succession of the Mino Belt, central Japan. A progressive environmental deterioration is evident from (1) a post-impact shutdown of burial flux of primary and silica- and apatite-secreting organisms; and (2) a subsequent abrupt increase in chemical weathering associated with a sustained reduction in the burial flux of radiolarian silica. No significant redox changes were observed across the impact event. The continental weathering proxies suggest a transient increase in weathering intensity occurred during the decline of radiolarian burial flux, likely in response to a short-term warm and humid period. Our results delineate a remarkable record of progressive environmental changes in the Panthalassa Ocean after this large impact event.

Keywords: Late Triassic, Norian, Bedded chert, Impact event, Environmental changes, Radiolaria

1 Introduction

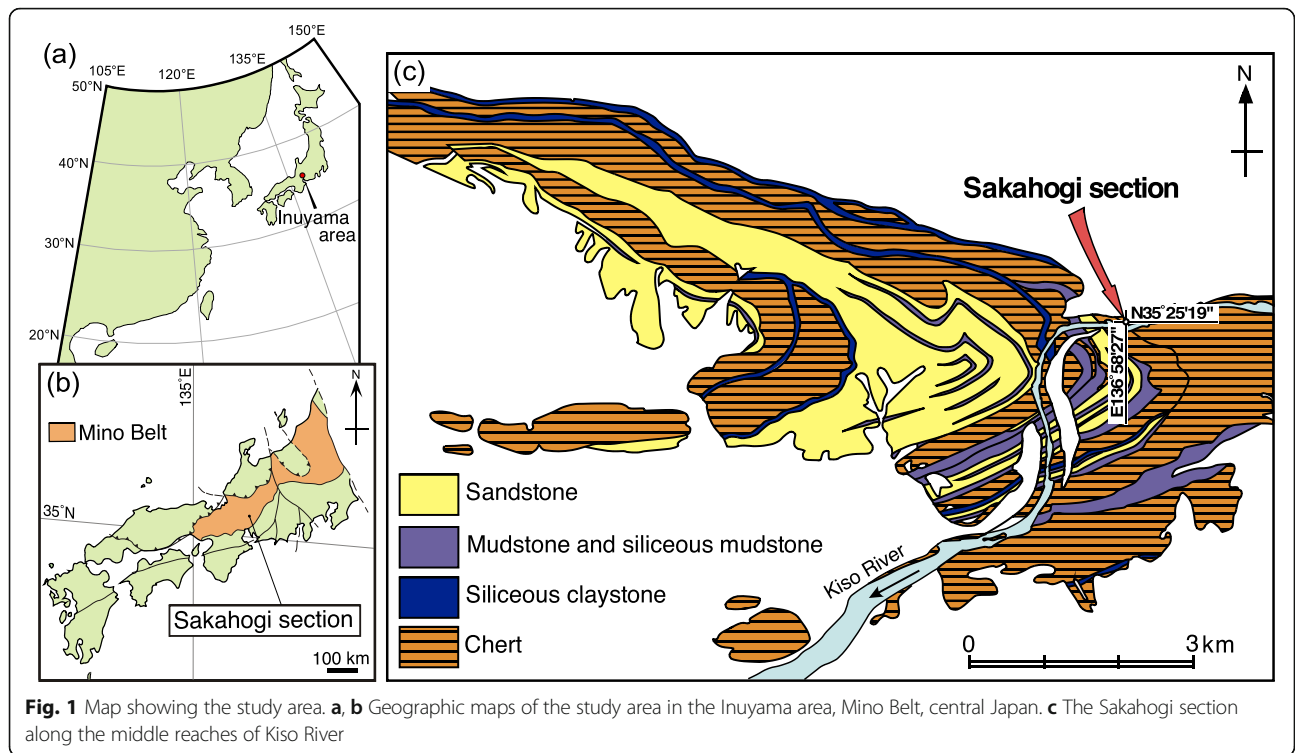
An Upper Triassic (Norian) impact event has been inferred from anomalous concentrations of platinum-group elements (PGEs) and a negative osmium (Os) isotope excursion, in addition to occurrences of microspherules and Ni-rich magnetite, in a claystone layer in an Upper Triassic bedded chert succession in the Sakahogi section, central Japan (Onoue et al. 2012; Sato et al. 2013; Sato et al. 2016) (Fig. 1). Previous paleomagnetic

studies of the Triassic bedded chert succession in the Sakahogi section suggest that these sediments accumulated in a pelagic, open-ocean setting within a low- to mid-latitude zone of the Panthalassa Ocean (Uno et al. 2015) (Fig. 2). The late middle Norian age of the claystone layer (Onoue et al. 2016a; Yamashita et al. 2018) suggests that the PGE anomalies originate from an extraterrestrial source, related to an impact event that formed the 90 km-diameter Manicouagan crater in Canada at 215.5 Ma (Clutson et al. 2018) (Fig. 2). Studies of PGEs and Os isotopes have revealed that the anomalously high PGE abundances in the lower sublayer claystone resulted from a large chondritic impactor with a diameter of 3.3–7.8 km (Sato et al. 2013; Sato et al. 2016).

* Correspondence: honami.sato@pchibakoudai.jp

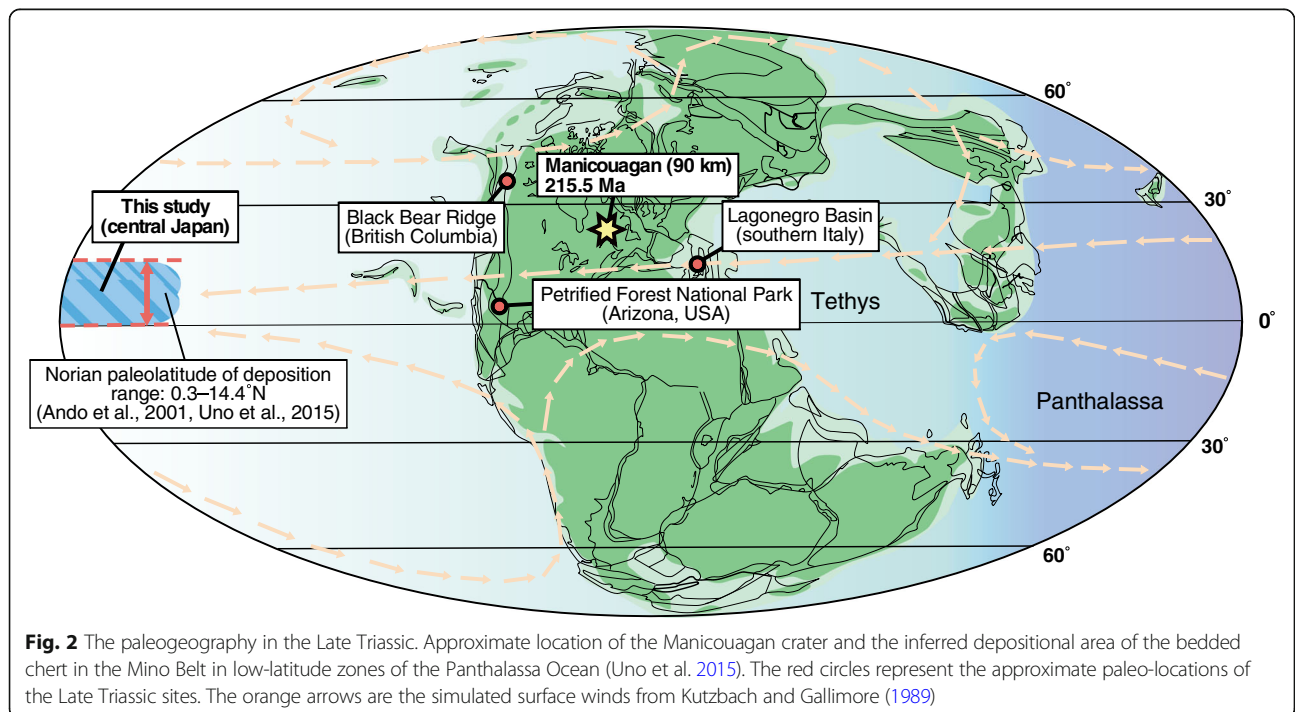
¹Ocean Resources Research Center for Next Generation, Chiba Institute of Technology, 2-17-1 Tsudanuma, Narashino, Chiba 275-0016, Japan

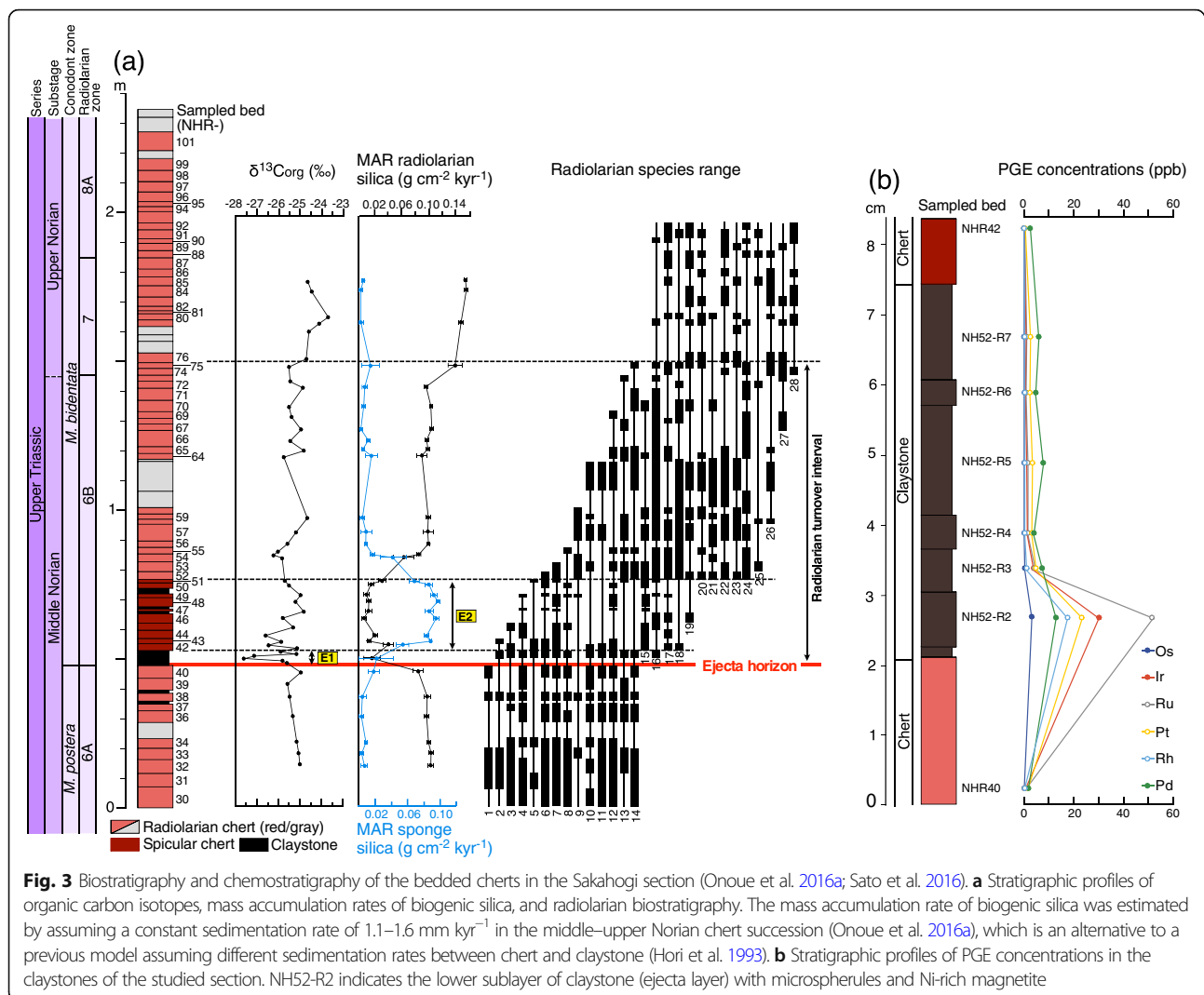
²Submarine Resources Research Center, Research Institute for Marine Resources Utilization, Japan Agency for Marine-Earth Science and Technology, 2-15 Natsushima-cho, Yokosuka, Kanagawa 237-0061, Japan
Full list of author information is available at the end of the article



Onoue et al. (2016a) showed that extinctions of middle Norian radiolarian species occurred in a stepwise fashion in the ~1 Myr interval above the ejecta horizon, which was associated with the radiation of late Norian radiolarians (Fig. 3a). Furthermore, high-resolution

paleontological and geochemical data also revealed that two paleoenvironmental events occurred during the initial phase of the radiolarian turnover interval. The first event (E1) involved post-impact shutdown of primary productivity reflected by a remarkable decline in the





amount of biogenic silica. The second event (E2) was characterized by a large and sustained reduction in the burial flux of radiolarian silica and the proliferation of siliceous sponges. This E2 event lasted until ~300 kyr after the impact. Although the relatively long period of the E2 interval (~300 kyr after the impact) largely excludes the possibility that the decline was triggered by instantaneous environmental stresses (e.g., extended darkness, global cooling, or acid rain) that would have been caused by a bolide impact, the primary cause of this decline remains uncertain.

In this study, we examined variations in the compositions of major, trace, and rare earth elements (REE) in bedded cherts in the Sakahogi section to identify the environmental changes responsible for the decline in radiolarian burial flux after the middle Norian impact event. The bedded cherts were composed originally of biogenic silica, apatite, barite, clastic lithogenic materials, and hydrogenous materials such as Fe–Mn oxides. The

geochemistry of the cherts has been extensively studied in the context of the depositional environment and global environmental change (e.g., Murray et al. 1992; Hori et al. 1993; Murray 1994; Kato et al. 2002; Takiguchi et al. 2006; Hori et al. 2007). The stratigraphic variations of major and trace elements in Triassic bedded cherts from Japanese accretionary complexes are widely used as proxies to trace changes in (1) hinterland components, (2) degree of chemical weathering in hinterland regions, (3) paleoproductivity, and (4) oceanic redox conditions. In this study, we assessed temporal variations in the compositions of major, trace, and rare earth elements (REE) in the Triassic bedded cherts to investigate the biotic responses to environmental changes that occurred after the impact event in the Panthalassa Ocean.

2 Geological setting and stratigraphy

The Mino Belt consists of Jurassic accretionary complexes in central Japan. The accretionary complexes in

the Mino Belt consist of two coherent units (i.e., the Samondake and Kamiaso units) and five melange units (i.e., the Sakamoto-toge, Funafuseyama, Kuze, Nabi, and Kanayama units). The coherent units consist of imbricate thrust sheets of sedimentary sequences that largely retain their primary stratigraphic coherency (e.g., Matsuda and Isozaki 1991; Isozaki 2014).

The study area in the Mino Belt is located in the Inuyama area, central Japan (Fig. 1). This area is in the southern part of the coherent Kamiaso Unit of the Mino Belt, which strikes E–W to NE–SW. The Kamiaso Unit in this area consists of thrust sheets of sedimentary sequences containing Triassic to Lower Jurassic bedded cherts and overlying Middle Jurassic clastic rocks (i.e., ocean plate stratigraphy; Isozaki 2014). The ocean plate stratigraphy is interpreted to have accumulated in a pelagic, deep-sea setting below the carbonate compensation depth and within a tapering wedge of distal, trench-fill turbidites at a subduction zone, respectively (Matsuda and Isozaki 1991). The absence of carbonate rocks and coarse-grained terrigenous material in the bedded cherts suggests that its primary depositional site was deeper than the carbonate compensation depth, and far beyond the transport distance of terrigenous clastic grains. Previous paleomagnetic studies of the Triassic bedded chert succession in the Mino Belt suggested that these sedimentary rocks accumulated in a pelagic, open-ocean setting within a low- to mid-latitudinal zone of the Panthalassa Ocean (Ando et al. 2001; Uno et al. 2015).

The Triassic to Jurassic cherts occur in 4 distinct thrust sheets named CH-1, -2, -3, and -4 in structurally ascending order (Yao et al. 1980). The Sakahogi section consists of a ~26 m-thick sequence of bedded cherts in the CH-2 thrust sheet. Individual chert beds in the Sakahogi section range in thickness from 1 to 10 cm, and are typically red to greenish gray, or occasionally white in color. The claystone layer in which PGE anomalies have been documented ranges in thickness from 4 to 5 cm and extends laterally for at least 90 m (Sato et al. 2016). The claystone comprises lower and upper sublayers (Onoue et al. 2012; Sato et al. 2013). The lower sublayer (NH52-R2) (Fig. 3b) contains microspherules within the clay mineral matrix (mainly illite), cryptocrystalline quartz, and hematite. The upper sublayer (NH52-R3 to NH52-R7) is composed of undisturbed clay minerals (illite) and cryptocrystalline quartz. The upper sublayer is further divided into five sub-categories based on variations in lithology, SiO₂ content, and relative abundance of biotic components (Sato et al. 2013). The SiO₂-rich sub-categories, NH52-R4 and NH52-R6, contain small amounts of radiolarians, sponge spicules, and conodonts.

Biostratigraphic and magnetostratigraphic studies (Sugiyama 1997; Onoue et al. 2012; Uno et al. 2015; Yamashita et al. 2018) have revealed that the claystone layer

occurs in upper middle Norian bedded chert. Given that the average sedimentation rate of the middle Norian chert, estimated from the measured thickness of the chert and the duration of deposition (Onoue et al. 2016a), is 1.1 mm kyr⁻¹, deposition of the claystone layer occurred ~1 Myr before the middle–upper Norian boundary (~214 Ma; Ogg 2012). Although the ages of substage boundaries in the Norian remain unclear due to a lack of reliable radio-isotopic dates and uncertainties in the magnetostratigraphic correlation between the Newark astrochronological polarity time scale (APTS) and marine-zoned strata (Ogg 2012), Onoue et al. (2016a) estimated the average sedimentation rate of the middle Norian chert based on the measured thickness (3.8 m) of the chert and the duration between the lower/middle (217.42 Ma) and middle/late Norian (213.97 Ma) boundaries (Ogg 2012).

3 Methods/Experimental

3.1 Major and trace elements analyses

To understand the environmental changes that triggered the decline in radiolarian burial flux after the middle Norian impact event, fifty-seven chert samples were collected across the ejecta layer for whole-rock geochemical analysis (Fig. 3). We also collected 6 claystone samples from the lower and upper sublayers. Veins and strongly recrystallized/weathered parts of the samples were avoided to minimize the effects of diagenetic and metamorphic overprinting on the sediment geochemistry. The chert and claystone samples were crushed, and the resulting fragments were carefully handpicked. These fragments were then powdered in an agate mortar and ball mill.

Major element (Ti, Al, Fe, Mn, K, and P) abundances were measured using a Rigaku ZSX Primus II X-ray fluorescence (XRF) spectrometer at the University of Tokyo, Japan, following the methods described by Kato et al. (1998) and Yasukawa et al. (2014). After drying the powdered samples at 110 °C for ~12 h, loss-on-ignition (LOI) values were calculated from the weight loss after ignition at 950 °C for >6 h. Fused glass beads for XRF analysis were made from a mixture of 0.400 g of ignited sample powder and 4.00 g of lithium tetraborate (Li₂B₄O₇) flux at ~1190 °C for 7 min in a Pt crucible. The standard data were generally within 3% (relative % difference) of accepted values for the reference basalt JB-2 (Imai et al. 1995), issued by the Geological Survey of Japan (GSJ).

Major (Mg, Ca, and Na), trace, and REE abundances were determined using an inductively coupled plasma quadrupole mass spectrometer (ICP–QMS; Agilent 7500c) at the University of Tokyo, following procedures described by Kato et al. (2005, 2011) and Yasukawa et al. (2014). After drying powdered samples at 110 °C for ~12

h, 0.100 g chert and 0.050 g claystone samples were dissolved by HNO₃–HF–HClO₄ digestion in tightly sealed Teflon PFA vessels, and then heated for several hours on a hot plate at 130 °C. The dissolved samples were progressively evaporated at 110 °C for 12 h, 160 °C for 3 h, and 190 °C until dryness. The residues were then dissolved in 4 mL of HNO₃ and 1 mL of HCl, and the solution was diluted to 1:1000 for the cherts and 1:2000 for the claystones (on a weight basis). Standard analyses were generally within 5% of the accepted values for JB-2 (Imai et al. 1995; Makishima and Nakamura 2006; Lu et al. 2007).

4 Results

4.1 Major and trace elements

Major and trace element data are listed in Tables 1, 2, and 3. Previous sedimentological and geochemical studies revealed that the chert beds in the Sakahogi section consist of SiO₂-diluted siliceous shale beds, reflecting fluctuations in radiolarian test abundances (Hori et al. 1993; Takiguchi et al. 2006; Sato et al. 2013). In fact, the chert bed samples contain > 90 wt.% SiO₂, which means the other major and trace elements are diluted by a large amount of biogenic silica. In particular, abundances of the major lithogenic elements, such as Al₂O₃, K₂O, and TiO₂, show a negative correlation with SiO₂ contents. This is attributed to dilution with nearly pure biogenic silica (e.g., radiolarians), as exemplified by the SiO₂–Al₂O₃, SiO₂–K₂O, and SiO₂–TiO₂ plots (Fig. 4). We assumed the SiO₂/Al₂O₃ ratio of terrigenous material in the Sakahogi section was 4.1, which is that of a sample with the highest Al₂O₃ content in the section (Fig. 4) and comparable to the ratio (~ 4.3) of upper continental crust (UCC; Rudnick and Gao 2014).

The data for the chert beds demonstrate that Al shows an excellent positive correlation with high-field-strength (HFS) elements such as Ti, Nb, Ta, and Th (Fig. 5). Considering the fact that Al, Ti, Nb, Ta, and Th are not significantly mobilized during post-depositional processes, including diagenesis and weathering, these correlations indicate that the majority of these elements are of detrital origin. The Ti/Al, Nb/Al, Ta/Al, and Th/Al ratios are identical to those of average UCC (Rudnick and Gao 2014) (Fig. 5). The present study also revealed that K and Rb correlate well with Al, Ti, Nb, Zr, Hf, and Th, but their Al-normalized ratios are different from those of UCC. In addition, Zr/Hf and Nb/Ta values obtained from chert and claystone samples show a strong linear correlation, and are comparable to those of average UCC (Fig. 6).

To avoid the significant dilution effect by biogenic SiO₂, concentrations of the elements were normalized to Al concentrations and compared with those of the UCC

(Rudnick and Gao 2014) to obtain enrichment factors. The enrichment factor is defined as follows:

$$X_{EF} = (X_{\text{sample}}/Al_{\text{sample}})/(X_{\text{UCC}}/Al_{\text{UCC}})$$

where X and Al are the concentrations of element X and Al, respectively. Furthermore, to minimize the possibility of diagenetic redistribution of elements from layers with lower SiO₂ content to adjacent layers with higher SiO₂ content (Tada 1991), we excluded the elemental data for non-detrital elements from SiO₂-poor parts of the claystone samples (NH52-R2, -R3, -R5, and -R7) when reconstructing the stratigraphic variations in enrichment factors.

Figures 7 and 8 show stratigraphic variations of enrichment factors for terrigenous elements, including HFS elements (Ti, Ta, Nb, Hf, and Zr) and alkali elements (K and Rb). Ti_{EF}, Nb_{EF}, and Ta_{EF} values are relatively constant throughout the studied section and close to a UCC value of 1. However, the lower sublayer claystone (NH52-R2) exhibits higher Ti_{EF} (~ 1.5) than those of other upper claystone and chert beds. Changes in Zr_{EF} and Hf_{EF} are also parallel to the UCC line in the studied interval. K_{EF} and Rb_{EF} vary between 1.12–1.75 and 1.6–2.4, respectively (Fig. 8). The K_{EF} and Rb_{EF} values decreased during the E2 event.

Vanadium, U, and Mo form highly soluble ions under oxygenated conditions, but under anoxic conditions, they are insoluble and in a lower valency state (Calvert and Pedersen 1993; Calvert and Pedersen 2007). Enrichment factors of these redox-sensitive elements are generally parallel to the UCC line in the studied interval (Fig. 7). Similarly, there are no significant changes in the enrichment factors of Ni and Zn (Table 2), which form highly insoluble sulfides under suboxic and/or anoxic bottom water conditions (Calvert and Pedersen 1993).

Si, Ca, Sr, P, and Ba are widely used as proxies for burial flux of biogenic material (Hollis 2003; Hollis et al. 2003; Takiguchi et al. 2006), based on their distribution in modern marine sediments (e.g., Schroeder et al. 1997). Stratigraphic variations of enrichment factors for these elements are shown in Fig. 7. Si_{EF} abruptly decreased during the initial E1 interval where the burial flux of silica-secreting radiolarians was markedly reduced (Onoue et al. 2016a). The trend in Ca_{EF} is similar to those of P_{EF} and Sr_{EF}, and there are strong positive correlations between Ca_{EF} and P_{EF} ($r = 0.93$) (Fig. 9). As with the Si_{EF} trend, there is an abrupt decrease in Ca_{EF}, P_{EF}, and Sr_{EF} during the initial E1 event, and these values began to rise after the E2 event. Ba_{EF} values also decreased sharply during the E1 interval, and were relatively constant after the E2 interval.

Table 1 Major element compositions of chert and claystone samples in the Sakahogi section

Sample ID	Lithology	Height (cm)	SiO ₂	TiO ₂	Al ₂ O ₃	Fe ₂ O ₃ *	MnO	MgO	CaO	Na ₂ O	K ₂ O	P ₂ O ₅	LOI	Total
NHR101	Chert	223.0	94.13	0.12	2.94	1.29	0.02	0.48	0.11	0.03	0.82	0.06	1.71	101.70
NHR99	Chert	215.1	95.96	0.09	2.21	0.87	0.03	0.30	0.09	0.03	0.57	0.04	1.11	101.31
NHR98	Chert	211.5	94.99	0.09	1.92	0.84	0.04	0.29	0.08	0.03	0.46	0.04	1.35	100.13
NHR97	Chert	207.9	95.56	0.10	2.28	0.87	0.03	0.29	0.08	0.03	0.59	0.04	1.04	100.89
NHR96	Chert	204.7	94.79	0.12	2.66	1.26	0.05	0.41	0.09	0.03	0.70	0.04	1.26	101.41
NHR95	Chert	202.5	95.00	0.10	2.14	1.19	0.02	0.32	0.11	0.03	0.58	0.06	1.47	101.02
NHR94	Chert	200.6	93.77	0.14	3.15	1.42	0.03	0.47	0.09	0.03	0.84	0.04	1.26	101.24
NHR92	Chert	195.0	94.68	0.09	2.06	1.04	0.02	0.34	0.11	0.03	0.53	0.05	1.51	100.45
NHR91	Chert	192.0	94.23	0.10	2.46	1.17	0.01	0.45	0.13	0.03	0.67	0.07	1.53	100.85
NHR90	Chert	190.0	94.17	0.10	2.77	1.32	0.01	0.51	0.12	0.03	0.76	0.06	1.48	101.32
NHR89	Chert	188.0	93.26	0.10	2.57	1.27	0.02	0.44	0.13	0.03	0.68	0.06	1.62	100.19
NHR88	Chert	186.0	92.29	0.14	3.36	1.63	0.02	0.61	0.13	0.04	0.91	0.06	1.82	101.00
NHR87	Chert	183.0	96.26	0.09	2.06	1.03	0.02	0.30	0.10	0.03	0.52	0.05	1.95	102.42
NHR86	Chert	179.0	95.52	0.09	2.09	0.97	0.02	0.31	0.09	0.03	0.54	0.04	1.45	101.15
NHR85	Chert	176.5	95.78	0.10	2.17	0.99	0.02	0.30	0.10	0.03	0.57	0.05	1.39	101.48
NHR84	Chert	173.0	95.22	0.10	2.35	1.09	0.02	0.38	0.09	0.03	0.60	0.04	1.50	101.42
NHR82	Chert	166.5	93.41	0.13	3.68	1.48	0.03	0.61	0.09	0.03	1.02	0.05	1.70	102.23
NHR81	Chert	165.0	94.67	0.10	2.60	1.07	0.02	0.47	0.10	0.03	0.68	0.04	1.66	101.44
NHR80	Chert	163.0	93.84	0.11	2.93	1.29	0.02	0.61	0.11	0.03	0.76	0.05	1.72	101.47
NHR76	Chert	151.0	94.85	0.10	2.28	1.11	0.02	0.36	0.09	0.03	0.64	0.04	1.56	101.07
NHR75	Chert	148.5	94.13	0.11	2.61	1.25	0.04	0.42	0.12	0.03	0.74	0.06	1.49	101.02
NHR74	Chert	146.3	94.47	0.13	3.06	1.41	0.02	0.43	0.13	0.03	0.86	0.08	1.41	102.03
NHR72	Chert	142.0	93.92	0.12	2.87	1.46	0.02	0.51	0.16	0.04	0.78	0.08	1.68	101.64
NHR71	Chert	138.9	95.33	0.12	2.60	1.14	0.02	0.34	0.12	0.03	0.72	0.08	1.20	101.70
NHR70	Chert	135.5	96.07	0.09	1.96	1.00	0.02	0.33	0.15	0.03	0.49	0.08	1.49	101.69
NHR69	Chert	132.0	95.68	0.09	2.27	1.08	0.02	0.48	0.16	0.03	0.57	0.07	1.51	101.96
NHR67	Chert	128.0	96.22	0.10	2.41	1.06	0.03	0.41	0.15	0.03	0.63	0.08	1.62	102.73
NHR66	Chert	124.5	95.16	0.11	2.39	1.17	0.02	0.32	0.14	0.03	0.65	0.08	1.54	101.61
NHR65	Chert	121.0	95.29	0.11	2.78	1.10	0.01	0.45	0.14	0.03	0.77	0.07	1.67	102.42
NHR64	Chert	119.0	95.13	0.11	2.60	1.15	0.02	0.42	0.12	0.03	0.71	0.06	1.67	102.02
NHR59	Chert	98.5	95.47	0.12	2.91	1.26	0.01	0.45	0.14	0.03	0.81	0.08	1.09	102.38
NHR57	Chert	93.0	96.97	0.11	2.35	1.15	0.05	0.36	0.13	0.03	0.62	0.07	1.03	102.87
NHR56	Chert	90.0	95.44	0.10	2.28	1.02	0.01	0.32	0.11	0.03	0.61	0.05	0.95	100.91
NHR55	Chert	87.0	96.31	0.09	2.21	0.91	0.01	0.33	0.10	0.03	0.58	0.05	1.02	101.63
NHR54	Chert	85.0	93.52	0.13	3.02	1.36	0.01	0.47	0.11	0.04	0.84	0.05	1.14	100.69

Table 1 Major element compositions of chert and claystone samples in the Sakahogi section (Continued)

Sample ID	Lithology	Height (cm)	SiO ₂	TiO ₂	Al ₂ O ₃	Fe ₂ O ₃ *	MnO	MgO	CaO	Na ₂ O	K ₂ O	P ₂ O ₅	LOI	Total
NHR53	Chert	82.0	94.21	0.12	2.57	1.15	0.01	0.39	0.10	0.03	0.70	0.04	1.03	100.35
NHR52	Chert	79.3	93.93	0.15	3.36	1.36	0.03	0.62	0.10	0.04	0.91	0.05	1.44	101.98
NHR51	Chert	77.5	93.23	0.15	3.39	1.62	0.02	0.57	0.13	0.04	0.95	0.06	1.27	101.41
NHR50	Chert	75.5	93.35	0.14	3.27	1.48	0.02	0.53	0.10	0.04	0.91	0.04	1.22	101.09
NHR49	Chert	72.5	93.11	0.14	3.32	1.55	0.02	0.57	0.11	0.04	0.95	0.04	1.19	101.03
NHR48	Chert	70.0	95.19	0.10	2.37	1.45	0.06	0.65	0.10	0.03	0.48	0.04	1.08	101.54
NHR47	Chert	67.5	93.04	0.15	3.72	1.64	0.03	0.78	0.12	0.04	0.95	0.05	1.32	101.84
NHR46	Chert	65.0	92.87	0.16	3.57	1.60	0.04	0.74	0.15	0.04	0.92	0.06	1.37	101.51
NHR44	Chert	59.0	95.81	0.14	3.05	1.08	0.02	0.47	0.12	0.04	0.80	0.06	1.14	102.72
NHR43	Chert	57.0	92.17	0.17	3.63	1.74	0.02	0.62	0.14	0.04	1.05	0.07	1.22	100.86
NHR42 upper	Chert	55.5	90.56	0.17	4.26	1.64	0.02	0.70	0.14	0.04	1.24	0.08	1.51	100.35
NHR42 lower	Chert	54.5	93.09	0.13	3.33	1.25	0.01	0.53	0.10	0.04	0.94	0.05	1.29	100.73
NH52R7	Claystone	53.5	77.48	0.50	10.33	5.38	0.05	1.87	0.20	0.07	3.27	0.12	2.71	101.97
NH52R6	Claystone	52.7	82.00	0.38	8.18	4.43	0.06	1.46	0.14	0.05	2.55	0.09	2.40	101.74
NH52R5	Claystone	51.7	70.62	0.64	13.52	7.04	0.07	2.34	0.30	0.09	4.31	0.18	3.26	102.36
NH52R4	Claystone	50.7	87.03	0.31	6.33	3.07	0.03	1.16	0.19	0.05	1.93	0.10	1.96	102.16
NH52R3	Claystone	50.2	65.84	0.81	15.95	8.50	0.11	2.85	0.40	0.10	4.98	0.27	3.83	103.63
NH52R2	Claystone (ejecta)	49.5	64.81	0.93	14.80	9.43	0.14	3.46	0.40	0.07	4.31	0.28	4.03	102.67
NHR40	Chert	47.0	93.12	0.13	2.94	1.38	0.02	0.50	0.10	0.03	0.83	0.05	1.13	100.22
NHR39	Chert	42.5	91.57	0.14	3.16	1.50	0.02	0.59	0.10	0.04	0.90	0.04	1.16	99.19
NHR38	Chert	38.0	92.48	0.13	3.00	1.45	0.02	0.61	0.10	0.03	0.80	0.04	1.13	99.78
NHR37	Chert	35.0	91.00	0.14	2.99	1.33	0.02	0.47	0.09	0.03	0.84	0.04	1.12	98.08
NHR36	Chert	32.0	90.42	0.14	3.28	1.46	0.03	0.57	0.09	0.04	0.91	0.04	1.20	98.17
NHR34	Chert	23.0	95.42	0.10	2.23	0.84	0.03	0.35	0.06	0.03	0.57	0.03	1.03	100.69
NHR33	Chert	19.5	95.17	0.10	2.37	0.95	0.11	0.34	0.06	0.03	0.62	0.03	0.93	100.71
NHR32	Chert	15.0	95.48	0.09	2.06	0.93	0.02	0.30	0.09	0.03	0.53	0.05	0.88	100.46
NHR31	Chert	10.5	94.60	0.10	2.29	0.94	0.02	0.34	0.08	0.03	0.62	0.03	0.93	99.99
NHR30	Chert	6.0	94.33	0.12	2.77	1.15	0.02	0.45	0.09	0.03	0.75	0.04	1.17	100.91

Concentration values presented are in wt.%. LOI loss on ignition. MgO, CaO, and Na₂O are corrected in oxide by ICP-MS data

Table 2 Trace element compositions of chert and claystone samples in the Sakahogi section

Sample ID	Lithology	Height (cm)	Sc	V	Cr	Co	Ni	Cu	Zn	Rb	Sr	Y	Zr	Nb	Mo	Cs	Ba	Hf	Ta	Pb	Th	U	Ni _{EF}	Zr _{EF}	Zr/Hf	Nb/Ta
NHR101	Chert	223.0	3.45	26.10	10.35	5.92	14.41	12.59	26.58	34.35	23.31	5.04	17.86	2.26	0.15	2.35	149.46	0.47	0.16	6.96	2.11	0.99	1.61	2.08	38.23	14.07
NHR99	Chert	215.1	3.14	14.45	8.17	3.68	10.54	17.87	18.02	25.63	23.25	5.38	12.81	1.73	0.12	1.61	159.05	0.35	0.12	4.08	1.51	0.49	1.56	1.88	37.03	14.42
NHR98	Chert	211.5	2.66	14.95	7.19	3.27	7.72	21.73	13.44	18.70	22.57	4.89	12.99	1.58	0.11	1.24	136.86	0.33	0.11	4.58	1.58	0.29	1.32	1.61	38.95	14.66
NHR97	Chert	207.9	3.49	13.61	9.37	3.88	11.47	17.76	17.58	25.76	22.93	4.61	13.60	1.90	0.08	1.61	157.72	0.37	0.13	3.67	1.69	0.31	1.65	1.78	36.37	14.51
NHR96	Chert	204.7	3.68	17.44	10.32	5.92	19.46	13.64	27.67	31.84	24.07	5.48	16.15	2.21	0.11	2.08	146.54	0.43	0.15	5.59	1.92	0.56	2.40	2.39	37.69	14.49
NHR95	Chert	202.5	3.50	19.24	7.86	3.33	8.64	15.80	13.73	23.03	23.93	5.12	15.87	1.74	0.15	1.55	149.84	0.41	0.12	6.83	1.70	0.52	1.32	1.48	38.47	13.98
NHR94	Chert	200.6	4.29	18.09	11.30	7.75	24.79	19.14	35.21	37.03	23.19	5.53	16.99	2.49	0.10	2.34	146.73	0.44	0.17	5.71	2.03	0.60	2.58	2.57	38.20	14.75
NHR92	Chert	195.0	2.76	18.64	7.08	4.34	10.85	13.22	16.53	22.43	23.79	4.71	14.79	1.61	0.11	1.55	135.06	0.37	0.11	6.67	1.60	0.60	1.72	1.84	39.87	14.17
NHR91	Chert	192.0	3.32	17.65	8.11	5.68	15.40	12.68	22.33	28.07	22.46	5.94	15.13	1.76	0.10	2.06	120.20	0.37	0.12	6.44	1.70	0.60	2.05	2.08	40.54	14.09
NHR90	Chert	190.0	3.60	19.17	8.98	6.07	16.37	13.49	24.16	30.99	22.93	5.78	17.07	1.93	0.10	2.46	129.94	0.40	0.13	6.24	1.92	0.87	1.94	2.01	42.52	14.31
NHR89	Chert	188.0	3.23	21.18	8.86	5.55	15.19	14.23	21.67	28.96	25.66	7.07	16.52	1.91	0.10	2.14	144.64	0.41	0.13	7.03	1.88	0.60	1.94	1.94	39.82	14.38
NHR88	Chert	186.0	4.31	26.06	11.78	7.62	21.34	14.07	30.40	38.18	24.50	6.99	21.80	2.54	0.11	2.98	143.84	0.54	0.18	7.09	2.55	0.67	2.08	2.08	40.09	14.15
NHR87	Chert	183.0	2.93	18.26	7.84	3.87	9.84	15.14	15.55	22.39	23.63	5.18	14.82	1.72	0.10	1.46	134.68	0.38	0.12	6.37	1.64	0.63	1.56	1.73	39.00	14.41
NHR86	Chert	179.0	3.13	17.50	7.77	3.81	9.96	18.04	16.22	22.91	24.56	4.63	16.10	1.75	0.08	1.52	141.49	0.40	0.12	5.67	1.70	0.45	1.56	1.79	40.04	14.45
NHR85	Chert	176.5	3.20	19.31	7.80	3.55	9.59	13.89	16.40	23.86	24.83	5.48	14.96	1.76	0.09	1.50	147.77	0.40	0.12	6.62	1.68	0.46	1.45	1.73	37.59	14.47
NHR84	Chert	173.0	3.45	19.37	8.45	5.24	12.98	13.38	21.14	25.28	25.12	5.12	16.31	1.91	0.09	1.67	151.93	0.41	0.13	6.47	1.78	0.65	1.81	2.07	39.48	14.28
NHR82	Chert	166.5	4.97	21.79	11.99	10.03	33.84	25.43	44.96	44.44	23.02	6.38	19.38	2.58	0.11	2.34	145.48	0.47	0.17	3.70	1.97	0.55	3.01	2.81	41.43	15.24
NHR81	Chert	165.0	3.66	21.19	8.70	5.95	14.97	24.28	23.76	29.49	26.10	5.06	17.05	1.98	0.07	2.06	153.09	0.41	0.14	3.68	1.79	0.93	1.89	2.10	41.79	14.28
NHR80	Chert	163.0	4.39	26.94	8.80	7.78	18.91	86.71	33.87	31.97	23.15	5.61	17.65	2.02	0.05	2.07	138.22	0.43	0.14	4.14	1.86	0.92	2.12	2.66	40.80	14.43
NHR76	Chert	151.0	4.06	20.47	8.35	3.77	11.16	15.77	18.01	28.63	23.96	5.20	19.64	2.09	0.07	1.96	140.88	0.47	0.14	5.83	1.73	0.79	1.61	1.82	42.06	15.43
NHR75	Chert	148.5	4.13	19.31	9.43	4.76	14.33	17.54	22.49	31.95	23.31	6.39	20.43	2.15	0.12	2.25	138.28	0.50	0.15	6.15	1.98	0.66	1.80	1.98	40.49	14.73
NHR74	Chert	146.3	4.38	17.01	11.60	5.53	19.70	17.41	26.88	38.78	25.60	9.39	18.66	2.52	0.13	2.34	141.71	0.48	0.16	6.61	1.99	0.73	2.11	2.02	39.21	15.46
NHR72	Chert	142.0	5.06	24.80	10.36	6.31	18.35	17.23	28.81	34.29	29.19	6.65	20.85	2.34	0.11	2.46	167.90	0.53	0.16	8.91	2.23	0.75	2.10	2.31	39.27	14.25
NHR71	Chert	138.9	4.49	17.62	10.80	4.35	14.29	11.98	24.05	32.94	26.80	5.56	17.62	2.30	0.11	2.05	163.03	0.47	0.15	6.59	1.94	0.66	1.80	2.13	37.85	15.01
NHR70	Chert	135.5	3.16	16.75	6.80	3.84	10.37	21.52	16.63	20.82	26.26	7.58	15.38	1.61	0.06	1.34	139.16	0.37	0.10	5.88	1.56	0.94	1.74	1.95	41.33	15.52
NHR69	Chert	132.0	3.74	19.98	7.84	6.25	17.14	16.75	27.78	27.55	27.68	9.16	17.30	1.87	0.06	1.67	155.79	0.41	0.12	6.24	1.71	1.04	2.47	2.81	42.68	15.59
NHR67	Chert	128.0	3.97	19.19	8.59	5.60	15.60	24.49	24.95	27.25	26.06	6.66	17.54	1.91	0.10	1.81	146.67	0.41	0.13	5.29	1.85	0.78	2.12	2.38	42.34	14.77
NHR66	Chert	124.5	4.36	23.43	8.27	4.21	10.98	20.30	17.39	26.50	25.80	6.51	18.48	2.00	0.09	1.77	149.74	0.49	0.14	6.64	2.15	0.67	1.50	1.67	37.66	14.26
NHR65	Chert	121.0	4.70	24.91	9.15	5.75	16.03	16.79	24.22	32.16	24.90	5.98	21.04	2.19	0.06	2.25	143.29	0.51	0.15	3.85	1.97	0.72	1.89	2.00	41.42	14.59
NHR64	Chert	119.0	4.40	19.99	9.33	5.42	15.16	81.63	26.13	29.82	25.08	5.95	20.97	2.16	0.08	2.20	156.91	0.50	0.15	4.87	1.93	0.72	1.91	2.31	41.77	14.78
NHR59	Chert	98.5	4.83	24.87	10.89	5.08	16.66	20.19	30.46	34.50	25.97	9.05	22.49	2.39	0.11	2.28	156.78	0.52	0.16	6.87	2.34	0.77	1.87	2.40	42.85	14.69
NHR57	Chert	93.0	4.21	20.63	9.08	4.21	12.49	18.01	20.62	27.33	27.00	7.68	18.93	2.09	0.11	1.89	152.72	0.48	0.14	6.69	1.94	0.78	1.74	2.01	39.65	14.66
NHR56	Chert	90.0	3.84	20.90	12.70	3.50	15.64	19.93	19.75	27.90	26.46	5.44	17.74	1.95	0.70	1.90	159.88	0.43	0.13	6.09	1.88	0.52	2.25	1.99	41.17	14.75
NHR55	Chert	87.0	3.42	16.80	8.40	3.54	12.17	15.35	21.73	26.55	24.10	5.22	16.94	1.84	0.11	1.94	148.77	0.41	0.12	4.36	1.73	0.90	1.80	2.26	41.40	14.95
NHR54	Chert	85.0	4.95	26.54	11.64	5.24	18.06	24.06	31.55	36.93	26.79	6.04	23.19	2.62	0.13	2.45	166.99	0.57	0.18	6.93	2.34	0.74	1.96	2.40	40.47	14.68

Table 2 Trace element compositions of chert and claystone samples in the Sakahogi section (Continued)

Sample ID	Lithology	Height (cm)	Sc	V	Cr	Co	Ni	Cu	Zn	Rb	Sr	Y	Zr	Nb	Mo	Cs	Ba	Hf	Ta	Pb	Th	U	Ni _{EF}	Zr _{EF}	Zr/Hf	Nb/Ta
NHR53	Chert	82.0	4.72	27.06	10.28	4.44	15.34	33.43	23.22	31.01	25.55	4.89	21.38	2.33	0.11	2.07	161.27	0.53	0.16	4.95	2.06	0.71	1.95	2.08	40.31	14.43
NHR52	Chert	79.3	5.97	29.13	17.29	7.03	24.92	34.90	45.62	39.86	23.70	5.99	21.34	3.03	0.11	2.31	171.87	0.56	0.20	3.77	2.22	0.52	2.43	3.12	37.99	15.08
NHR51	Chert	77.5	5.82	34.42	12.51	6.60	24.06	30.61	35.09	41.24	28.38	6.54	26.86	2.98	0.13	2.99	175.72	0.69	0.21	7.08	2.59	0.63	2.32	2.38	38.94	14.27
NHR50	Chert	75.5	4.96	23.83	11.88	5.58	20.86	24.67	31.18	40.34	25.86	6.66	25.71	2.70	0.11	2.89	170.49	0.60	0.19	5.68	2.38	0.72	2.09	2.19	42.96	14.54
NHR49	Chert	72.5	5.53	24.75	12.63	6.04	22.89	30.04	38.81	43.57	26.52	7.09	24.92	2.80	0.11	3.07	170.07	0.57	0.19	6.93	2.43	0.84	2.26	2.69	43.49	14.75
NHR48	Chert	70.0	4.09	18.52	8.93	5.28	17.33	50.30	32.54	21.70	23.58	6.05	16.29	1.97	0.09	1.41	141.24	0.41	0.13	4.55	1.71	0.57	2.40	3.16	39.99	15.04
NHR47	Chert	67.5	6.22	25.63	12.94	7.77	31.22	30.09	49.99	42.71	26.51	7.69	26.46	3.02	0.09	2.83	169.23	0.65	0.21	3.43	2.59	0.66	2.75	3.09	40.68	14.25
NHR46	Chert	65.0	6.89	22.28	14.20	6.67	28.97	36.83	40.58	41.51	28.60	10.30	27.06	3.17	0.14	2.97	174.91	0.66	0.22	6.09	2.82	0.61	2.66	2.61	40.73	14.63
NHR44	Chert	59.0	5.56	18.75	11.89	4.69	21.50	38.56	29.44	34.53	28.27	9.74	23.31	2.62	0.12	2.29	175.81	0.59	0.18	3.54	2.55	0.58	2.31	2.22	39.26	14.41
NHR43	Chert	57.0	7.10	34.64	15.84	6.45	24.00	32.49	33.13	46.91	27.78	10.83	32.14	3.57	0.19	3.22	171.29	0.76	0.24	6.30	3.24	0.78	2.17	2.10	42.40	14.66
NHR42 upper	Chert	55.5	7.07	32.50	15.60	7.34	34.71	23.31	44.78	53.57	27.14	15.31	31.53	3.60	0.12	3.64	169.45	0.77	0.24	5.31	3.18	0.48	2.67	2.42	40.86	14.70
NHR42 lower	Chert	54.5	5.60	25.38	11.96	5.27	26.38	18.94	32.23	40.82	26.24	11.12	27.42	2.71	0.09	2.83	166.67	0.61	0.19	4.82	2.45	0.63	2.60	2.22	44.98	14.44
NH52R7	Claystone	53.5	18.91	83.22	43.93	19.51	81.71	22.97	112.18	137.64	29.49	20.01	80.92	10.06	0.31	9.61	214.80	2.05	0.71	14.37	8.74	1.34	2.59	2.50	39.47	14.21
NH52R6	Claystone	52.7	12.55	59.13	34.95	15.59	65.02	17.94	86.61	105.31	23.19	14.50	61.74	7.49	0.25	7.50	188.16	1.54	0.53	13.14	6.45	1.07	2.60	2.43	40.17	14.27
NH52R5	Claystone	51.7	22.97	99.76	56.54	25.29	112.18	21.63	138.37	173.31	34.40	24.90	80.93	12.44	0.40	12.40	238.29	2.08	0.86	17.37	10.44	1.56	2.72	2.35	39.00	14.45
NH52R4	Claystone	50.7	11.26	46.41	29.92	13.51	60.50	15.49	71.94	84.04	25.54	15.39	49.73	5.99	0.17	5.63	177.04	1.16	0.42	10.07	5.26	0.82	3.13	2.61	42.82	14.38
NH52R3	Claystone	50.2	28.07	115.77	77.68	32.04	145.85	18.97	175.90	193.83	41.00	31.00	101.90	14.76	0.47	12.03	257.96	2.53	1.05	18.71	12.32	1.92	3.00	2.54	40.24	14.10
NH52R2	Claystone (ejecta)	49.5	30.16	99.36	475.90	44.32	325.94	17.23	337.24	181.74	32.53	23.47	76.23	10.48	0.35	8.90	185.65	2.15	0.71	16.39	7.91	1.36	7.21	5.24	35.48	14.69
NHR40	Chert	47.0	5.19	30.01	11.96	5.32	21.11	26.86	27.75	36.83	23.59	7.40	24.89	2.68	0.21	2.97	150.60	0.61	0.19	7.06	2.46	0.87	2.36	2.17	41.06	14.08
NHR39	Chert	42.5	6.35	27.26	11.85	7.34	27.23	15.44	36.85	40.10	25.15	6.98	23.62	2.72	0.13	3.31	163.12	0.65	0.20	7.43	2.69	0.72	2.83	2.68	36.50	13.87
NHR38	Chert	38.0	5.05	28.29	11.83	9.74	29.66	29.34	42.28	35.68	24.21	6.39	21.77	2.53	0.12	2.94	157.59	0.55	0.18	6.65	2.45	0.80	3.24	3.24	39.33	13.93
NHR37	Chert	35.0	5.79	25.30	11.41	5.84	20.36	83.47	27.02	35.54	24.02	6.41	23.55	2.63	0.10	2.77	155.96	0.61	0.19	5.20	2.53	0.65	2.23	2.08	38.50	13.88
NHR36	Chert	32.0	5.59	26.75	12.32	8.95	29.26	113.25	37.33	37.98	24.15	6.19	23.11	2.74	0.13	2.93	158.08	0.60	0.20	5.00	2.61	0.79	2.93	2.62	38.68	13.97
NHR34	Chert	23.0	3.79	19.05	8.96	3.93	11.18	22.88	16.88	23.70	21.41	4.26	17.02	1.89	0.11	1.46	142.03	0.46	0.14	3.70	1.80	0.71	1.64	1.74	37.35	13.94
NHR33	Chert	19.5	3.55	19.61	8.15	4.23	11.50	26.52	19.01	24.54	20.90	4.16	17.60	1.82	0.07	1.48	139.77	0.43	0.13	4.18	1.72	0.67	1.59	1.84	40.63	13.75
NHR32	Chert	15.0	4.55	19.11	8.03	3.81	10.93	13.77	17.84	21.74	22.09	5.57	17.47	1.74	0.08	1.37	140.95	0.43	0.12	4.98	1.77	0.96	1.74	2.00	40.89	14.15
NHR31	Chert	10.5	4.62	21.58	8.42	4.44	13.58	30.04	20.31	25.71	21.78	5.77	18.70	1.81	0.08	1.66	147.91	0.45	0.12	4.01	1.76	0.93	1.94	2.04	41.73	14.78
NHR30	Chert	6.0	6.45	22.94	10.79	5.83	18.11	32.02	26.69	32.51	24.03	6.91	24.79	2.42	0.08	2.22	162.59	0.60	0.17	5.51	2.23	0.70	2.14	2.21	41.43	14.03

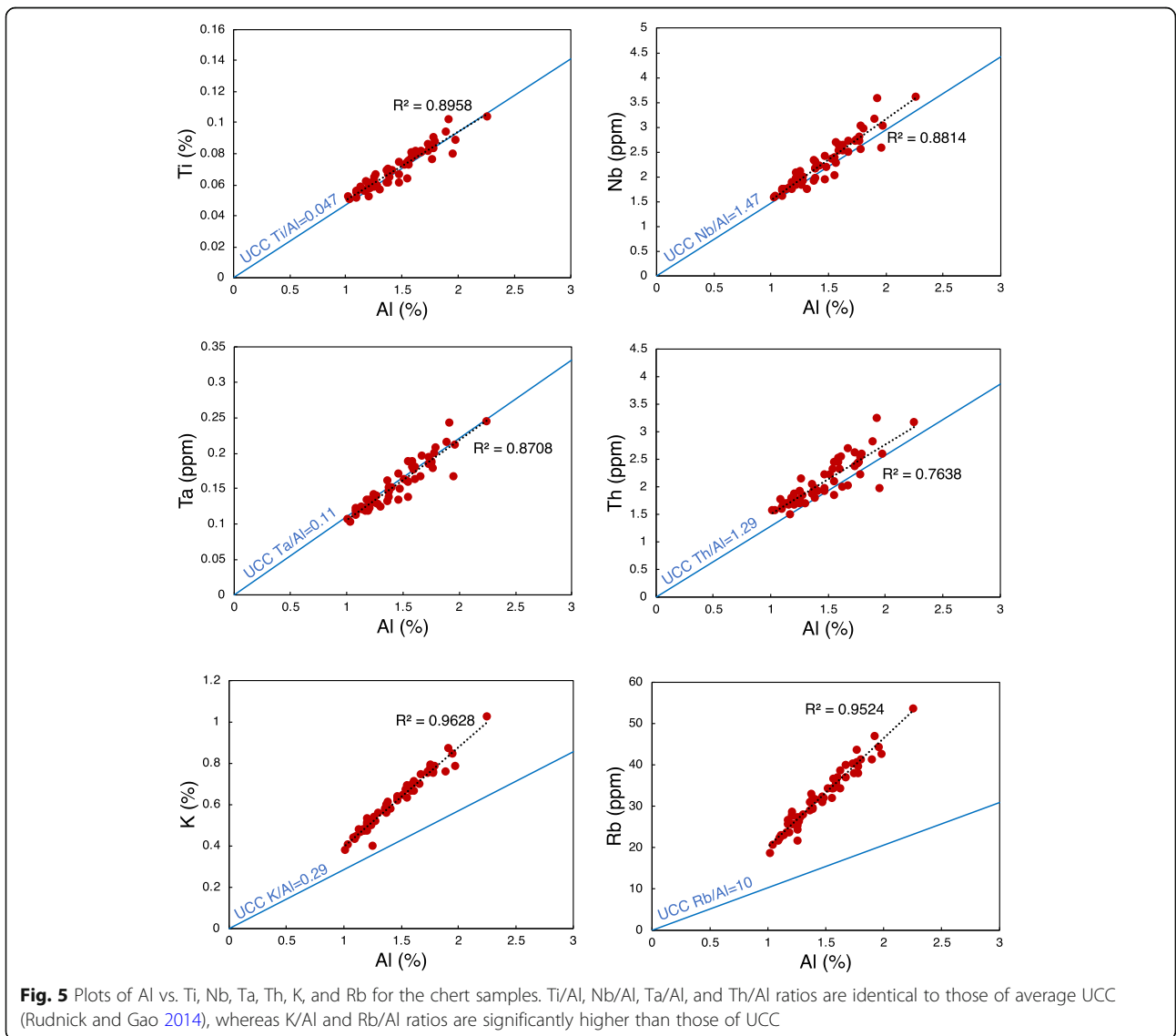
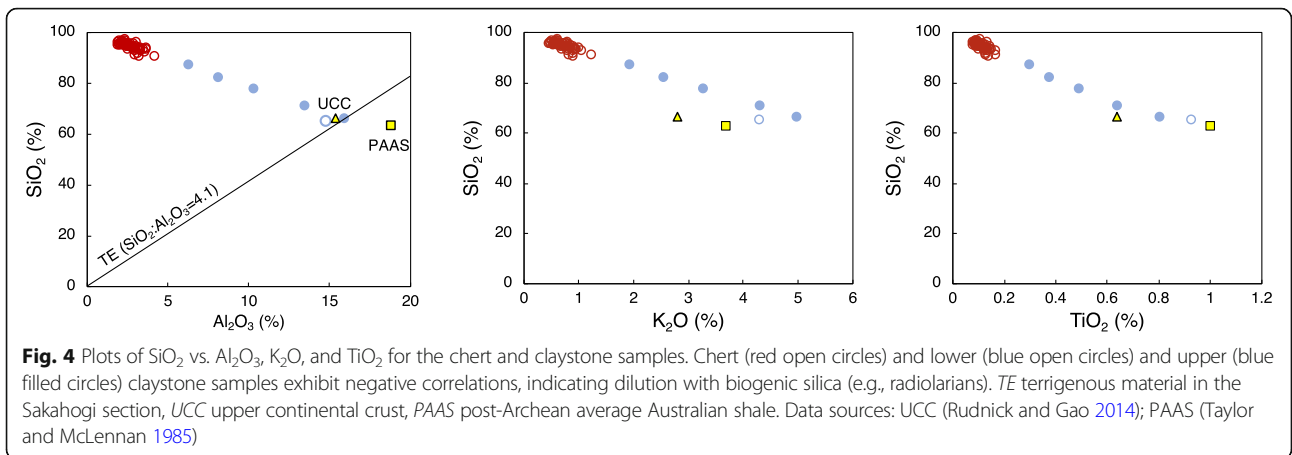
Concentration values presented are in mg/g

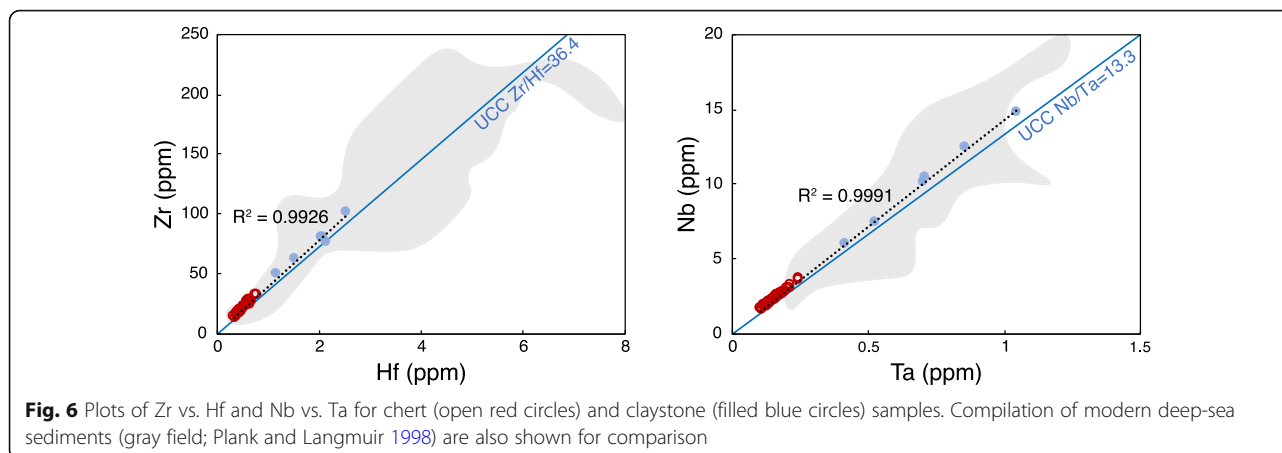
Table 3 Rare earth element compositions of chert and claystone samples in the Sakahogi section

Sample ID	Lithology	Height (cm)	La	Ce	Pr	Nd	Sm	Eu	Gd	Tb	Dy	Ho	Er	Tm	Yb	Lu	ΣREE_{Ef}	MREE/MREE*	Ce/Ce*	Eu/Eu*
NHR101	Chert	223.0	6.26	18.29	1.50	5.62	1.09	0.23	0.97	0.15	0.92	0.18	0.55	0.08	0.54	0.09	1.29	0.87	1.41	0.95
NHR99	Chert	215.1	5.49	15.51	1.39	5.27	1.07	0.23	1.04	0.15	0.90	0.17	0.51	0.07	0.48	0.07	1.52	0.78	1.32	0.95
NHR98	Chert	211.5	4.78	14.64	1.27	5.01	1.07	0.24	1.03	0.16	0.93	0.18	0.51	0.07	0.45	0.07	1.65	0.68	1.40	0.99
NHR97	Chert	207.9	5.14	15.37	1.29	5.08	1.01	0.22	0.95	0.14	0.82	0.16	0.44	0.06	0.40	0.06	1.42	0.77	1.41	0.97
NHR96	Chert	204.7	5.98	17.80	1.50	5.81	1.18	0.26	1.10	0.17	1.03	0.19	0.54	0.07	0.49	0.07	1.41	0.77	1.40	1.00
NHR95	Chert	202.5	5.28	14.68	1.34	5.14	1.10	0.25	1.05	0.16	0.97	0.19	0.54	0.08	0.50	0.08	1.52	0.73	1.30	0.99
NHR94	Chert	200.6	6.45	20.22	1.73	6.77	1.39	0.29	1.26	0.18	1.05	0.20	0.55	0.07	0.49	0.07	1.35	0.70	1.42	0.96
NHR92	Chert	195.0	4.85	14.85	1.28	4.98	1.07	0.23	1.01	0.15	0.89	0.18	0.50	0.07	0.46	0.07	1.54	0.69	1.40	0.97
NHR91	Chert	192.0	5.95	18.01	1.60	6.22	1.32	0.29	1.26	0.19	1.12	0.22	0.60	0.09	0.55	0.08	1.58	0.68	1.37	0.97
NHR90	Chert	190.0	5.94	17.61	1.58	6.16	1.30	0.29	1.21	0.18	1.05	0.20	0.58	0.08	0.52	0.08	1.38	0.69	1.35	0.99
NHR89	Chert	188.0	6.53	19.65	1.78	7.06	1.51	0.34	1.54	0.22	1.30	0.25	0.69	0.10	0.60	0.09	1.68	0.66	1.35	0.96
NHR88	Chert	186.0	7.61	23.41	1.94	7.38	1.50	0.33	1.40	0.21	1.27	0.25	0.72	0.10	0.66	0.10	1.45	0.77	1.43	0.98
NHR87	Chert	183.0	5.44	16.39	1.42	5.45	1.17	0.26	1.10	0.17	0.96	0.19	0.53	0.07	0.48	0.07	1.70	0.71	1.39	0.98
NHR86	Chert	179.0	4.86	14.37	1.28	4.93	1.04	0.23	0.98	0.15	0.88	0.17	0.48	0.07	0.44	0.07	1.49	0.71	1.36	0.99
NHR85	Chert	176.5	5.60	15.83	1.49	5.76	1.22	0.28	1.21	0.18	1.05	0.20	0.58	0.08	0.51	0.08	1.63	0.69	1.29	0.98
NHR84	Chert	173.0	5.73	16.59	1.50	5.78	1.21	0.27	1.16	0.17	0.99	0.19	0.54	0.08	0.48	0.07	1.54	0.72	1.33	0.98
NHR82	Chert	166.5	7.34	20.72	1.88	7.27	1.42	0.31	1.34	0.19	1.17	0.22	0.63	0.09	0.59	0.08	1.22	0.78	1.31	0.98
NHR81	Chert	165.0	5.58	17.09	1.53	5.96	1.25	0.28	1.16	0.18	1.01	0.20	0.53	0.07	0.47	0.07	1.41	0.68	1.37	1.01
NHR80	Chert	163.0	6.31	17.62	1.75	6.68	1.41	0.30	1.27	0.20	1.13	0.22	0.60	0.08	0.54	0.08	1.36	0.68	1.24	0.98
NHR76	Chert	151.0	5.30	16.56	1.42	5.43	1.15	0.25	1.06	0.16	0.95	0.19	0.54	0.08	0.50	0.08	1.54	0.70	1.42	0.98
NHR75	Chert	148.5	6.14	19.06	1.60	6.27	1.34	0.28	1.25	0.19	1.15	0.23	0.68	0.10	0.62	0.09	1.55	0.70	1.43	0.95
NHR74	Chert	146.3	8.67	24.94	2.36	9.21	1.91	0.44	1.96	0.28	1.62	0.31	0.84	0.11	0.74	0.10	1.82	0.69	1.29	0.99
NHR72	Chert	142.0	6.82	21.79	1.84	7.13	1.51	0.34	1.43	0.22	1.26	0.24	0.68	0.10	0.62	0.09	1.60	0.68	1.44	0.99
NHR71	Chert	138.9	6.14	19.22	1.57	6.06	1.28	0.29	1.17	0.17	1.00	0.18	0.52	0.07	0.51	0.08	1.53	0.73	1.46	1.02
NHR70	Chert	135.5	6.53	18.39	1.84	7.29	1.62	0.37	1.67	0.24	1.39	0.28	0.74	0.10	0.64	0.10	2.19	0.61	1.24	0.96
NHR69	Chert	132.0	7.30	20.81	1.98	7.86	1.71	0.38	1.69	0.25	1.51	0.30	0.84	0.12	0.77	0.12	2.09	0.65	1.28	0.97
NHR67	Chert	128.0	6.32	20.24	1.63	6.27	1.36	0.30	1.27	0.19	1.14	0.23	0.66	0.10	0.63	0.10	1.74	0.71	1.48	0.98
NHR66	Chert	124.5	7.06	21.55	1.86	7.21	1.56	0.34	1.43	0.21	1.26	0.24	0.68	0.10	0.62	0.10	1.92	0.68	1.40	0.97
NHR65	Chert	121.0	6.17	18.72	1.58	6.04	1.27	0.28	1.19	0.19	1.12	0.22	0.64	0.09	0.59	0.09	1.43	0.74	1.41	0.99
NHR64	Chert	119.0	6.46	18.36	1.67	6.46	1.37	0.31	1.33	0.20	1.20	0.23	0.63	0.09	0.57	0.08	1.56	0.71	1.31	0.98
NHR59	Chert	98.5	8.04	21.14	2.15	8.52	1.81	0.40	1.75	0.26	1.54	0.31	0.88	0.12	0.80	0.12	1.71	0.67	1.19	0.98
NHR57	Chert	93.0	7.01	20.33	1.76	6.78	1.44	0.32	1.38	0.21	1.24	0.25	0.72	0.10	0.68	0.10	1.87	0.74	1.36	0.98
NHR56	Chert	90.0	5.89	20.73	1.51	5.73	1.23	0.27	1.12	0.17	1.00	0.19	0.55	0.08	0.52	0.08	1.78	0.73	1.63	1.00

Table 3 Rare earth element compositions of chert and claystone samples in the Sakahogi section (Continued)

Sample ID	Lithology	Height (cm)	La	Ce	Pr	Nd	Sm	Eu	Gd	Tb	Dy	Ho	Er	Tm	Yb	Lu	ΣREE_{Ef}	MREE/MREE*	Ce/Ce*	Eu/Eu*
NHR55	Chert	87.0	5.54	19.45	1.51	5.90	1.28	0.28	1.17	0.18	1.02	0.19	0.53	0.07	0.47	0.07	1.77	0.66	1.58	1.00
NHR54	Chert	85.0	6.79	23.79	1.82	7.01	1.48	0.31	1.36	0.20	1.18	0.23	0.63	0.09	0.57	0.09	1.57	0.70	1.59	0.95
NHR53	Chert	82.0	5.63	19.26	1.48	5.58	1.19	0.26	1.07	0.16	0.97	0.19	0.52	0.07	0.47	0.07	1.49	0.72	1.57	0.98
NHR52	Chert	79.3	7.52	23.62	1.95	7.53	1.51	0.33	1.35	0.19	1.13	0.22	0.59	0.08	0.55	0.08	1.44	0.75	1.45	0.99
NHR51	Chert	77.5	7.89	25.32	2.05	7.82	1.66	0.36	1.51	0.23	1.29	0.26	0.70	0.11	0.65	0.10	1.53	0.72	1.48	1.00
NHR50	Chert	75.5	6.90	22.29	1.94	7.59	1.63	0.36	1.58	0.23	1.32	0.25	0.69	0.10	0.61	0.09	1.45	0.64	1.43	0.97
NHR49	Chert	72.5	7.14	22.59	1.94	7.50	1.65	0.36	1.60	0.24	1.35	0.26	0.72	0.10	0.63	0.09	1.45	0.66	1.42	0.97
NHR48	Chert	70.0	5.86	17.42	1.65	6.67	1.53	0.34	1.48	0.23	1.18	0.22	0.59	0.08	0.53	0.08	1.66	0.58	1.31	0.99
NHR47	Chert	67.5	7.60	20.75	2.05	8.04	1.72	0.38	1.63	0.24	1.39	0.27	0.78	0.11	0.71	0.11	1.28	0.67	1.23	0.98
NHR46	Chert	65.0	9.72	25.48	2.53	9.97	2.19	0.49	2.19	0.31	1.78	0.36	0.99	0.14	0.87	0.13	1.66	0.67	1.21	0.97
NHR44	Chert	59.0	8.58	22.46	2.37	9.43	2.13	0.50	2.07	0.30	1.72	0.33	0.93	0.13	0.82	0.12	1.77	0.61	1.17	1.04
NHR43	Chert	57.0	10.41	26.19	2.73	10.82	2.34	0.52	2.24	0.33	1.93	0.38	1.08	0.15	0.99	0.15	1.73	0.68	1.15	0.98
NHR42 upper	Chert	55.5	13.15	33.11	3.61	14.39	3.23	0.76	3.35	0.49	2.79	0.53	1.49	0.20	1.23	0.18	1.92	0.62	1.13	1.00
NHR42 lower	Chert	54.5	8.12	20.70	2.39	9.64	2.24	0.55	2.42	0.37	2.12	0.39	1.06	0.14	0.85	0.12	1.60	0.55	1.10	1.02
NH52R7	Claystone	53.5	26.66	72.52	6.90	26.17	5.07	1.01	4.22	0.61	3.63	0.74	2.16	0.32	2.08	0.32	1.53	0.80	1.26	0.94
NH52R6	Claystone	52.7	19.19	52.82	4.97	19.05	3.62	0.74	3.06	0.45	2.73	0.56	1.66	0.24	1.58	0.24	1.41	0.80	1.27	0.97
NH52R5	Claystone	51.7	34.58	92.59	9.24	35.96	7.27	1.51	6.11	0.87	4.86	0.94	2.67	0.38	2.47	0.37	1.54	0.72	1.22	0.98
NH52R4	Claystone	50.7	17.45	46.12	4.75	18.70	3.94	0.84	3.55	0.51	2.98	0.58	1.68	0.24	1.53	0.23	1.69	0.67	1.19	0.97
NH52R3	Claystone	50.2	44.94	113.80	11.72	45.92	9.31	1.96	7.86	1.08	6.14	1.19	3.40	0.49	3.19	0.48	1.64	0.73	1.17	0.99
NH52R2	Claystone (ejecta)	49.5	30.73	79.55	8.33	33.46	7.32	1.63	6.60	0.90	4.85	0.90	2.46	0.34	2.19	0.33	1.26	0.64	1.17	1.02
NHR40	Chert	47.0	7.49	22.50	2.18	8.59	1.96	0.44	1.82	0.27	1.51	0.28	0.78	0.11	0.69	0.10	1.73	0.58	1.30	1.00
NHR39	Chert	42.5	8.20	27.08	2.47	9.78	2.21	0.49	1.99	0.30	1.53	0.28	0.73	0.10	0.63	0.09	1.84	0.56	1.40	1.01
NHR38	Chert	38.0	7.59	24.97	2.33	9.28	2.14	0.48	1.97	0.27	1.44	0.26	0.67	0.09	0.56	0.08	1.81	0.54	1.38	1.01
NHR37	Chert	35.0	8.40	26.15	2.53	10.04	2.23	0.49	1.96	0.29	1.46	0.26	0.70	0.10	0.59	0.09	1.92	0.57	1.32	1.02
NHR36	Chert	32.0	8.45	25.30	2.52	9.94	2.20	0.47	1.91	0.27	1.46	0.27	0.69	0.09	0.61	0.09	1.72	0.58	1.28	1.00
NHR34	Chert	23.0	5.80	17.71	1.61	6.32	1.38	0.29	1.20	0.18	0.98	0.18	0.48	0.07	0.41	0.06	1.71	0.64	1.36	0.98
NHR33	Chert	19.5	5.87	17.95	1.61	6.23	1.34	0.28	1.17	0.17	0.99	0.18	0.47	0.06	0.41	0.06	1.61	0.67	1.37	0.97
NHR32	Chert	15.0	6.63	19.09	2.08	8.30	1.89	0.41	1.73	0.24	1.28	0.22	0.58	0.08	0.46	0.07	2.18	0.53	1.20	0.98
NHR31	Chert	10.5	6.11	18.45	1.81	7.22	1.70	0.37	1.61	0.23	1.26	0.22	0.59	0.08	0.48	0.07	1.83	0.55	1.30	0.98
NHR30	Chert	6.0	7.65	24.08	2.32	9.17	2.03	0.45	1.87	0.27	1.49	0.27	0.71	0.09	0.57	0.08	1.92	0.57	1.33	1.00





4.2 Rare earth elements

Table 3 lists the REE concentrations of the chert and claystone samples in the studied section. Enrichment factors of the total REE concentrations ($\Sigma\text{REE}_{\text{EF}}$) have positive correlations with Ca_{EF} and P_{EF} and are also positively correlated with some trace elements, such as Zr_{EF} , Hf_{EF} , and Th_{EF} (Fig. 9). Figure 10 shows the REE patterns of chert and claystone beds across the impact ejecta layer normalized to UCC (Rudnick and Gao 2014). Enrichment of the middle REEs (MREEs; Sm, Gd, Tb, and Dy) exhibits stratigraphic changes. The chert beds throughout the whole section are relatively enriched in MREEs, whereas REE patterns for the claystones (NH52-R2 to R7) are relatively flat with nearly UCC values (Fig. 10). To calculate the relative MREE enrichments, UCC-normalized MREE/MREE* ratios were used (Chen et al. 2015):

$$\text{MREE}/\text{MREE}^* = \frac{2 \times (\text{avg. MREE}/\text{avg. MREE}_{\text{UCC}})}{(\text{avg. LREE}/\text{avg. LREE}_{\text{UCC}}) + (\text{avg. HREE}/\text{avg. HREE}_{\text{UCC}})}$$

where LREE and HREE represent light REEs (La, Ce, Pr, and Nd) and heavy REEs (Er, Tm, Yb, and Lu) respectively.

The MREE/MREE* ratios across the ejecta layer show a decrease in MREE enrichment after the impact event. The average MREE/MREE* ratio in cherts below the ejecta layer is 1.35, whereas in the E1 interval it is 1.12. The MREE/MREE* ratios rapidly increase in the chert beds of the E2 interval, indicating a pronounced decline in MREE enrichment during the E1 interval.

Ce and Eu are the only two REEs that have multiple valence states, which results in fractionation that can be quantified by Ce and Eu anomalies (German and Elderfield 1989; German and Elderfield 1990; Holser 1997). Cerium and Eu anomalies are calculated as:

$$\text{Ce}/\text{Ce}^* = 2\text{Ce}_N / (\text{La}_N + \text{Pr}_N)$$

$$\text{Eu}/\text{Eu}^* = 2\text{Eu}_N / (\text{Sm}_N + \text{Gd}_N)$$

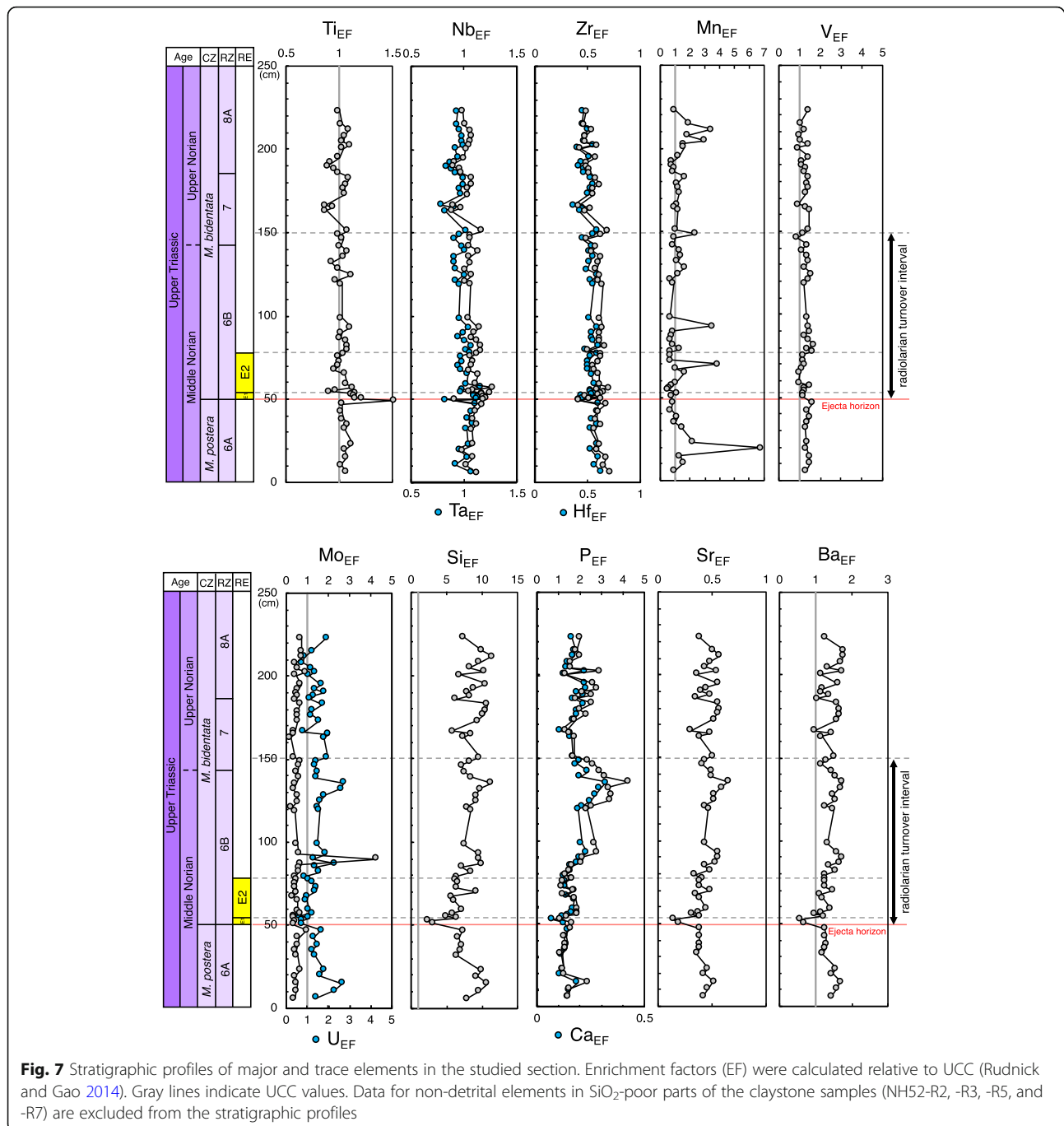
The subscript “N” denotes UCC-normalized values. Ce/Ce* values exhibit positive anomalies and vary from 1.10–1.63 throughout the studied section (Fig. 11). Ce/Ce* values fluctuate during the radiolarian turnover interval (Fig. 11), but are essentially uniform after this interval. There are no Eu anomalies relative to UCC through the studied section (Fig. 10). The average Eu/Eu* value of the studied section is 0.98 ± 0.02 .

5 Discussion

On the basis of high-resolution profiles of biogeochemical signatures (Si, Ba, Ca, and P), redox-sensitive elements, REE, and Chemical Index of Alteration (CIA; Nesbitt and Young 1982) values obtained from the Triassic bedded cherts, we assessed the environmental changes that triggered a decline in radiolarian burial flux after the Norian impact event. Here, we consider three of the main environmental changes (paleoproductivity, oceanic redox conditions, and provenance) before discussing the triggers for the decline in radiolarian burial flux based on these controls.

5.1 Paleoproductivity

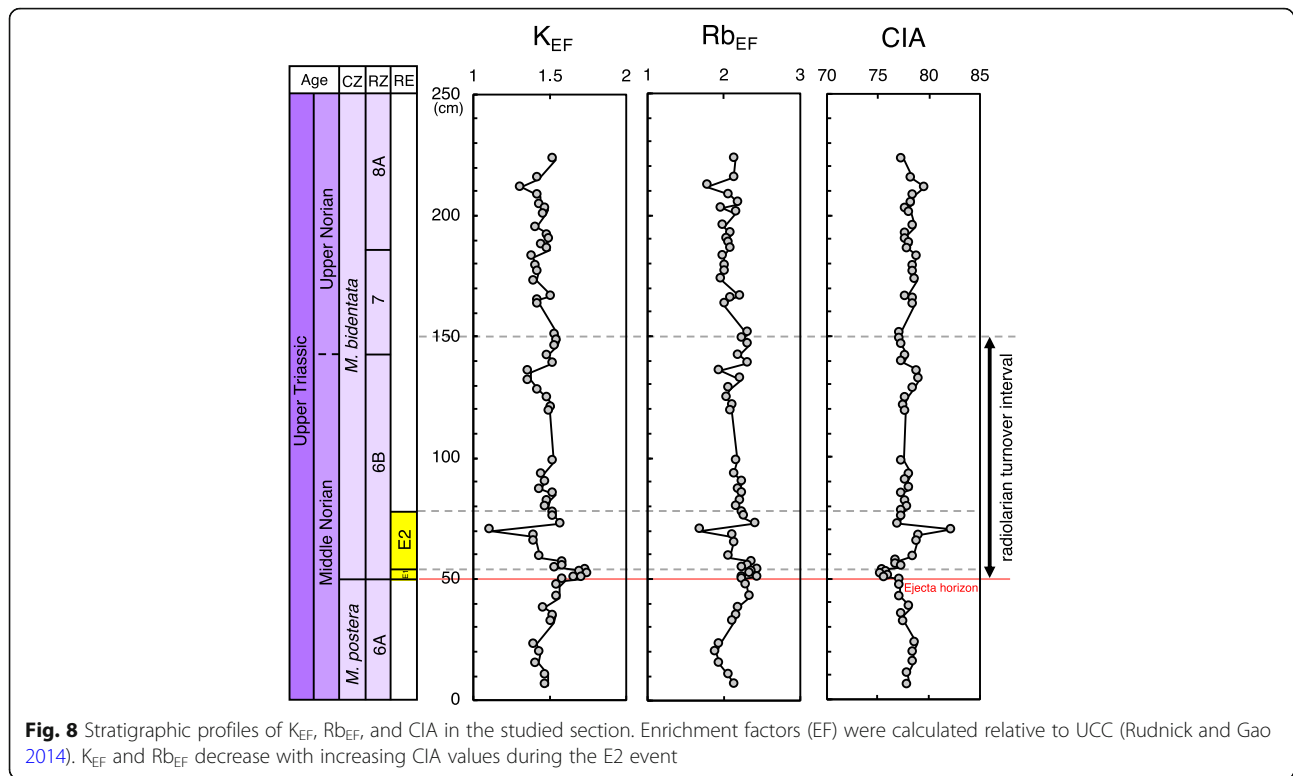
Changes in marine primary productivity may have played an important role at the base of the marine food chain after the middle Norian impact event. A post-impact reduction in primary productivity has been suggested based on the negative $\delta^{13}\text{C}_{\text{org}}$ excursion observed during the E1 event (Onoue et al. 2016a). To evaluate productivity estimates based on $\delta^{13}\text{C}_{\text{org}}$ data, we used Ba_{EF} as another proxy for primary productivity. It is generally considered that barite precipitation occurs in decaying particulate organic matter while it sinks to the



seafloor (Dehairs et al. 1980; Bishop 1988; Dymond and Collier 1996). Enhanced Ba_{EF} values below high-productivity areas support this assumption (Nürnberg et al. 1997). Given that pore water in a sediment column is generally saturated with respect to barite, the barite associated with productivity can be preserved after burial. Therefore, the Ba_{EF} record of the bedded cherts can be used as a proxy for productivity variations in the surface ocean (e.g., Zachos et al. 1989; Dymond and Collier

1996; McManus et al. 1998; Algeo et al. 2011). Our data show that Ba_{EF} in the studied section decreases in the E1 interval and recovers in the E2 interval. The stratigraphic profile of Ba_{EF} mimics that of δ¹³C_{org}, which supports the previous interpretation of δ¹³C_{org} records that marine primary productivity decreased in the E1 interval and recovered in the E2 interval (Onoue et al. 2016a).

Phosphorous is also a geochemical proxy for paleoproductivity in pelagic deep-sea sediments (e.g., Murray and



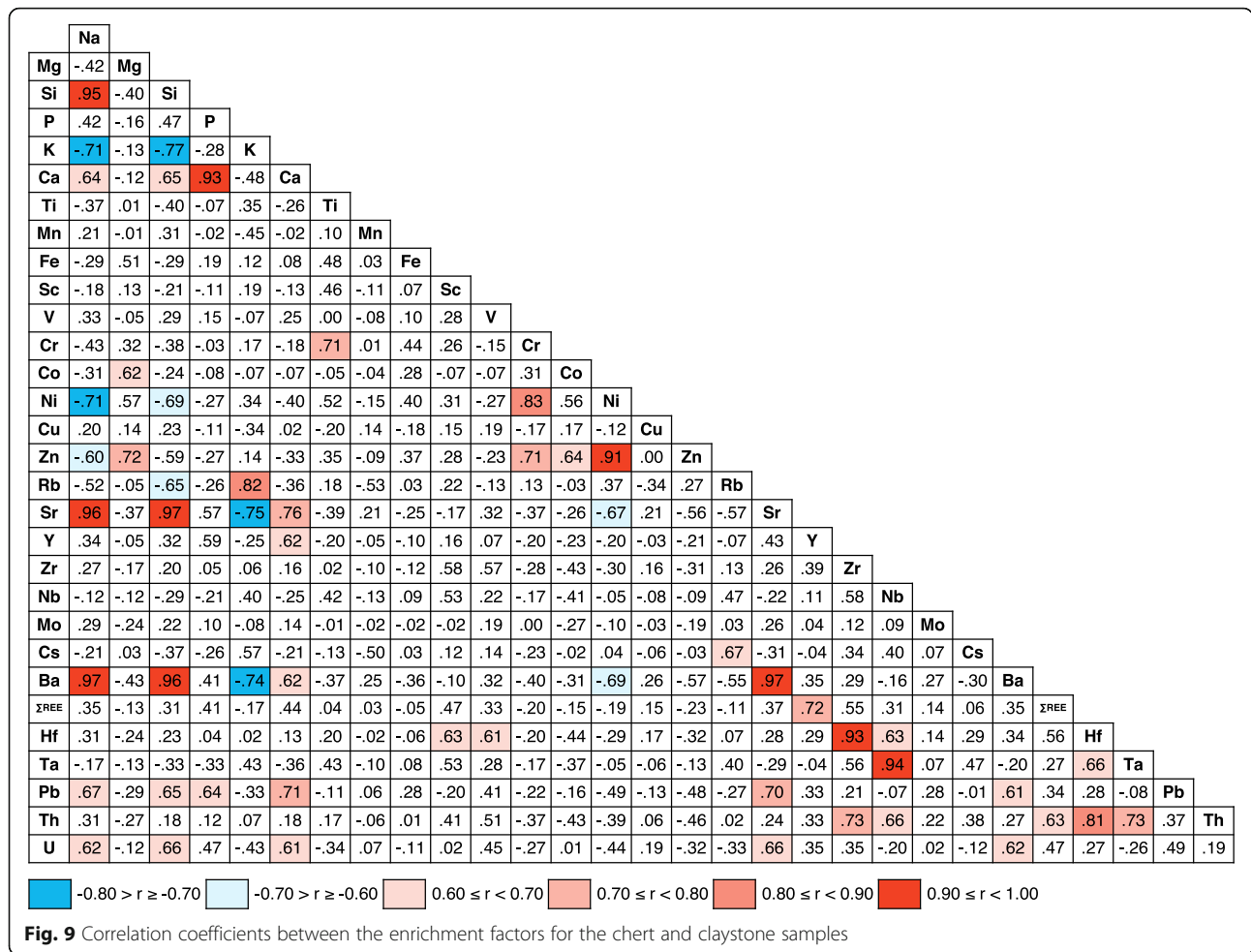
Leinen 1993; Algeo et al. 2011). Phosphorous is transferred to the sediment mainly as organically bound P, most of which is subsequently liberated through remineralization of organic matter; long-term retention of P in sediment requires adsorption onto ferric oxyhydroxide and subsequent mineralization as authigenic phosphates (Algeo and Ingall 2007). For our samples, a strong positive correlation between P_{EF} and Ca_{EF} ($r = 0.93$) implies that the apatite species is the main host phase for P. P_2O_5/CaO ratios of Triassic conodonts, or biogenic apatite, obtained from a bedded chert succession in Inuyama area range from 0.71 to 0.77 with an average of 0.74 (Takiguchi et al. 2006). The P_2O_5/CaO obtained from our samples is almost identical ($P_2O_5/CaO = 0.72$) to those of conodonts. These data suggest that biogenic apatite such as conodonts is preserved in our samples as the main carrier of Ca and P. Thus, P_{EF} cannot be used as a proxy for primary productivity in the studied section, but instead P_{EF} and Ca_{EF} reflect biogenic apatite (i.e., conodonts) accumulation relative to terrigenous accumulation in the bedded cherts.

The stratigraphic variations in Ca_{EF} and P_{EF} indicate that the accumulation of biogenic apatite decreased during the E1 interval, whereas its accumulation recovered after the E2 interval (Fig. 7). Strontium is geochemically similar to Ca and may replace Ca in apatite, which is supported by the positive correlation between Sr_{EF} and Ca_{EF} ($r = 0.76$). Significant negative excursions in Sr_{EF} in

the E1 interval may also reflect a decrease in biogenic apatite accumulation.

Additional information regarding changes in biogenic apatite accumulation may be derived from REE data. The UCC-normalized REE patterns of the bulk chert samples show slight MREE enrichment (Fig. 10), which is probably due to the presence of fossil biogenic apatite that recrystallized during diagenetic processes (Reynard et al. 1999; Chen et al. 2015). The claystones in the E1 interval have similar LREE and HREE abundances, but slightly different MREE abundances, resulting in a flatter pattern in that interval. Relative depletion of MREEs in the claystone samples is probably due to the paucity of conodont fossils, which is consistent with the interpretation that the decrease in Ca_{EF} and P_{EF} was associated with decreased accumulation of biogenic apatite during the E1 interval.

The oxygen isotopic composition of conodont apatite derived from Late Triassic deep-marine sediment sections in the western Tethys has revealed that conodont $\delta^{18}O$ values reflect surface water temperatures and that these conodonts lived in near-surface waters (Rigo and Joachimski 2010; Rigo et al. 2012). Thus, significant negative excursions in Ca_{EF} and P_{EF} in the E1 interval may reflect a decrease in biogenic apatite accumulation by conodonts in near-surface waters in a pelagic realm of the Panthalassa Ocean. $\delta^{13}C_{org}$ and Ba_{EF} data also imply that primary productivity in the pelagic



Panthalassa was also decreased during the E1 interval. We infer that the decimation of conodonts in this oceanic region was likely to have been related to the collapse of primary productivity. Following the resurgence in primary productivity after the E1 event, the biogenic apatite content proxies had recovered to pre-impact values by the first chert bed overlying the claystone layer, which suggests conodonts had begun to recover after the E1 event.

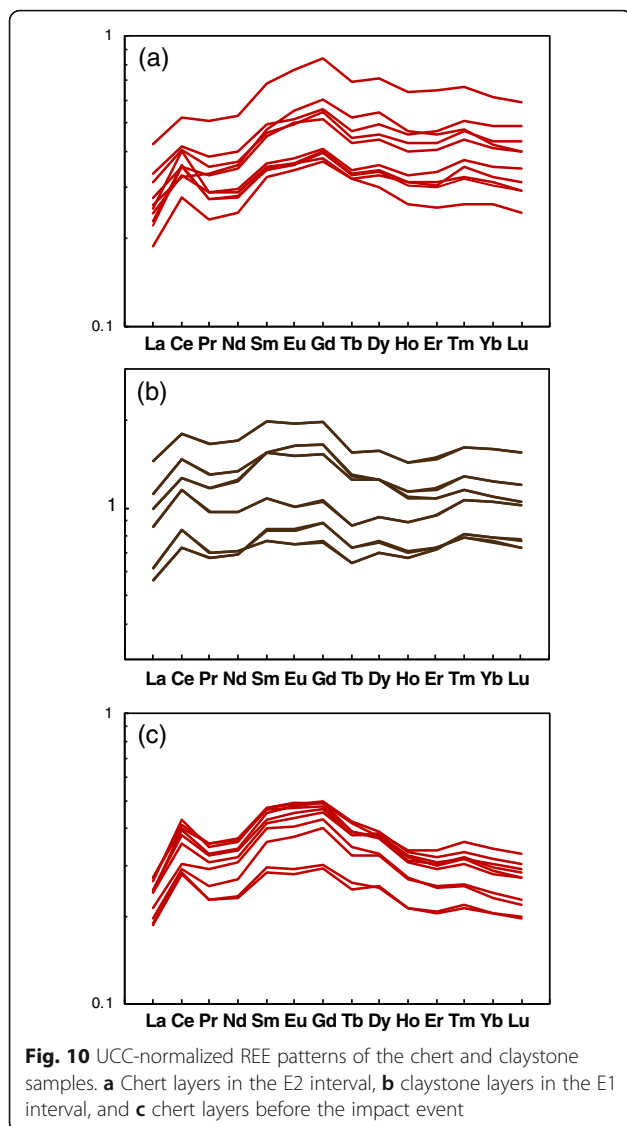
In contrast, radiolarian burial flux did not recover until the E2 event, which was 300 kyr after the impact event (Onoue et al. 2016a). To account for the sustained reduction in the burial flux of radiolarian silica during the E1 and E2 events, the factors controlling radiolarian burial flux (e.g., availability of dissolved silica and seawater temperature; De Wever et al. 2014) are discussed below.

5.2 Redox change

Elements such as Mn, V, U, and Mo are useful to constrain ancient oceanic redox conditions (Tribouillard et al. 2006), because their valency can vary as a function

of the prevailing redox potential (Calvert and Pedersen 1993; Calvert and Pedersen 2007). We discuss the sedimentary redox changes through the studied section using the following proxies for redox conditions.

Manganese is one of the most commonly used geochemical proxies for redox conditions in the oceanic environment. It forms insoluble Mn(III) or Mn(IV) hydroxides or oxides (e.g., MnO₂) that are deposited rapidly in particulate form (Calvert and Pedersen 1993; Sholkovitz et al. 1994). However, under anoxic conditions, Mn is reduced to Mn(II) and forms soluble cations (e.g., Mn²⁺ and MnCl⁺). Consequently, a small enrichment factor for Mn (Mn_{EF}) in marine sediments suggests reducing depositional conditions near the surface of the sediments. In the studied section, Mn_{EF} generally fluctuates (0.55–1.95) around a UCC value of 1, except for several high-Mn_{EF} peaks (Mn_{EF} > 2, Fig. 7). Although it is possible that these high-Mn_{EF} peaks could reflect diagenetic enrichment of Mn, their origin remains unclear. Compared with the general trend of Mn_{EF} in Upper Triassic bedded cherts in the Sakahogi section (Nozaki et al. 2019), the Mn_{EF} values in the studied section are lower than the average value of the



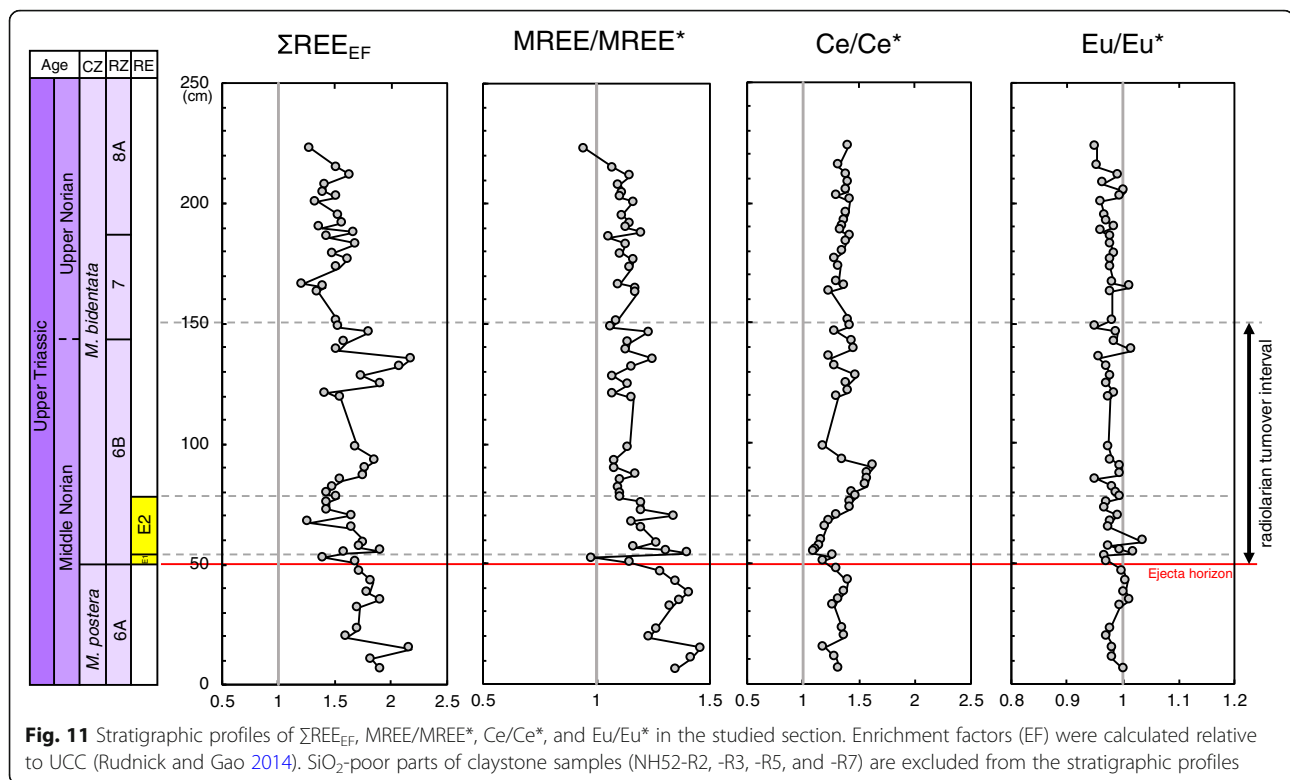
entire Norian Stage ($Mn_{EF} = 3.00$; $n = 35$). However, significant redox changes across the ejecta layer cannot be recognized from Mn.

Vanadium and U enrichments in sediments are useful proxies for reducing depositional conditions, ranging from moderately to strongly reducing (Sadiq 1988; Algeo and Maynard 2004; Tribouillard et al. 2006). Vanadium and U reduction in seawater occurs under Eh conditions close to that required for the reduction of Fe(III) to Fe(II), which is lower than that for Mn reduction (Takeno 2005). In oxic seawater, V is present as soluble V(V) in the quasi-conservative form of vanadate oxyanions (HVO_4^{2-} and $H_2VO_4^-$). When conditions change from oxic to mildly reducing, V(V) converts to V(IV) and forms the vanadyl ion (VO^{2+}), related hydroxyl species ($VO(OH)_3^-$), and insoluble hydroxides ($VO(OH)_2$) (Breit and Wanty 1991; Wanty and

Goldhaber 1992). Under such reducing conditions, soluble U(VI) is reduced to insoluble U(IV). In the studied section, V_{EF} values show constant low values across the ejecta layer (0.88–1.67) and are similar to UCC values throughout the studied section (Fig. 7). U_{EF} is higher than that of UCC, but its values are low (1.02–2.73) compared with U_{EF} in modern anoxic–sulfidic basins (~ 5 ; Algeo and Tribouillard 2009) and a period of anoxia in the Anisian reported from the Sakahogi section (Nozaki et al. 2019). The V and U data demonstrate that the redox conditions in the studied section were stable and oxic across the impact event. We further examined the redox conditions based on the enrichment of Mo, but Mo_{EF} is constantly low or similar to UCC values in the studied section, except for one outlier at 90.0 cm (Fig. 7).

The Ce anomaly is also a common tracer for redox conditions in pelagic sediments (e.g., Kato et al. 2002; Fujisaki et al. 2016; Nozaki et al. 2019). Given that Ce is relatively insoluble in seawater following oxidation from Ce(III) to Ce(IV), it responds to redox changes in seawater (Sholkovitz et al. 1992). Authigenic carbonate and phosphate minerals are considered to record seawater REE chemistry (Toyoda and Tokonami 1990; Kamber and Webb 2001). However, in the studied section, the chert samples consist of a mixture of biogenic silica and detrital materials. Therefore, Ce_{EF} in the chert samples may reflect both seawater and detrital components, whereas in the claystones could be dominated by components from detrital material rather than from seawater. Ce/Ce^* values in the studied section range from 1.10 to 1.63, and generally show a relatively constant value of ~ 1.4 (Fig. 11). The slightly positive Ce anomaly ($Ce/Ce^* > 1$) throughout the studied section could be attributable to the provenance of detrital components (discussed in next subsection), as reflected by the different K/Al and Rb/Al ratios as compared with average UCC (Fig. 5). Hence, our results suggest that Ce/Ce^* values of the studied section mainly record the detrital signature. However, the Ce/Ce^* variation in this study is much narrower than that during the late Permian oceanic anoxia event (Kato et al. 2002) and the period of acidic conditions at the end-Triassic (Hori et al. 2007), which again implies that there was no significant redox change at this pelagic site due to the Late Triassic impact event.

Our analysis of redox-sensitive elements cannot detect any redox change in the equatorial region of the Panthalassa Ocean across the Late Triassic impact event. Redox conditions along the Panthalassan coast of the western Pangean supercontinent have been studied throughout the Upper Triassic to Lower Jurassic interval in the Black Bear Ridge section, British Columbia (Sephton et al. 2002; Wignall et al. 2007; Onoue et al. 2016b) (Fig. 2). The redox-sensitive



elements show there was no redox change in the middle to late Norian (Wignall et al. 2007). In the western Tethys Ocean, Upper Triassic carbonate sequences of the Lagonegro Basin, southern Italy (Fig. 2) have been examined for redox changes using Mo and U enrichments and Ce/Ce^* anomalies. Redox changes in the middle to upper Norian interval have not been detected (Casacci et al. 2016). In summary, the Norian impact did not appear to induce redox changes in the Panthalassa and western Tethys oceans, although this interpretation requires further geochemical study at other middle to late Norian sites.

5.3 Changes in dust provenance or hydrological cycle

The HFS (Ti, Zr, Hf, Nb, and Ta) and alkali (K and Rb) elements are largely contained in detrital phases in the Triassic bedded chert sequences of the Inuyama area (Hori et al. 2000; Soda and Onoue 2019). These detrital components were transported to a pelagic setting in a low-latitude region of the Panthalassa Ocean (Uno et al. 2015), mainly as eolian dust or aerosols (Hori et al. 1993). According to model simulations of the surface winds (Kutzbach and Gallimore 1989), dust delivered to the depositional area of the bedded cherts in the Inuyama area largely originated from a low-latitude

zone of western Pangea (Nakada et al. 2014; Ikeda et al. 2017) (Fig. 2).

The enrichments of HFS elements are relatively constant throughout the studied section and close to a UCC value of 1. This suggests that UCC-like terrigenous material was the source for these elements throughout the whole section. Given that different terrestrial reservoirs have characteristic Zr/Hf and Nb/Ta ratios, and there is no significant fractionation of these ratios by continental weathering or sedimentation processes, Nb/Ta and Zr/Hf can be used to constrain the source of these elements in sediments (Pfänder et al. 2007; Berndt et al. 2011). In the Sakahogi section, both the chert and claystone samples have typical UCC ratios (Pfänder et al. 2007), with $\text{Zr}/\text{Hf} = 40.1 \pm 1.9$ (chert; $n = 57$) and 39.5 ± 2.4 (claystone; $n = 6$), and $\text{Nb}/\text{Ta} = 14.5 \pm 0.4$ and 14.4 ± 0.2 (Table 2), respectively. In addition, Zr/Hf and Nb/Ta values in the Sakahogi section show a strong linear correlation ($R^2 > 0.99$, Fig. 6) compared with the values in modern deep-sea sediments (e.g., Plank and Langmuir 1998). These data suggest that typical UCC-like terrigenous material was the principal detrital components throughout the Sakahogi section. Alternatively, if the values of Zr/Hf and Nb/Ta were similar in wide area of hinterland in Pangea, the potential change in provenance of eolian dust cannot be ruled out. Actually, changes in dust provenance that occurred during Norian in Fundy

Basin, North America, are suggested based on reappearance of eolian deposits on various timescale (Kent and Olsen 2000). Notably, the lower sublayer claystone (NH52-R2) exhibits lower Zr_{EF} , Hf_{EF} , Nb_{EF} , and Ta_{EF} , and higher Ti_{EF} than those of the other upper claystone samples and cherts. This is most likely explained by contamination of ejecta materials in the lower sublayer.

Concentrations of K and Rb correlate well with those of Al and HFS elements, which indicate that these alkali elements are of terrigenous origin. Potassium, Rb, and Al contents are attributed to aluminosilicates, especially clay minerals. Given that Al is resistant to chemical weathering (Nesbitt and Young 1982), Al-normalized K and Rb can be used as chemical weathering indicators (Tanaka and Watanabe 2015; Grygar et al. 2019; Liu et al. 2019). In the present study, the enrichment factors of K and Rb show similar trends. The stratigraphic variations in K_{EF} and Rb_{EF} show an obvious decreasing trend during the E2 event (Fig. 8), which suggest the intensity of aluminosilicate chemical weathering increased during the E2 event.

To assess the degree of chemical weathering in hinterland regions using major elements, we calculated the Chemical Index of Alteration (CIA; Nesbitt and Young 1982). Values of CIA predict the extent of decomposition of feldspar minerals, which are the most abundant mineral group in the UCC. Before calculating CIA values, apatite-derived CaO concentrations were corrected using the procedure of Price and Velbel (2003). This correction estimates CaO in the silicate phase (CaO*) by subtracting CaO in the phosphate phase predicted from the P_2O_5 concentration and stoichiometry of apatite:

$$CaO^* = molCaO - [(10/3) \times molP_2O_5]$$

CIA was then calculated as:

$$CIA^* = Al_2O_3 / (Al_2O_3 + Na_2O + K_2O + CaO^*) \times 100$$

CIA values vary between 75–82 in the studied section (Fig. 8). CIA values are relatively constant below the ejecta layer, slightly decrease in the E1 interval, and then increase in the E2 interval (especially in sample for NHR48). These stratigraphic variations in CIA values indicate intensified chemical weathering on continents during the E2 interval, implying that the climate changed to relatively warm and humid conditions after the impact event. K_{EF} and Rb_{EF} values decrease with increasing CIA values, indicating that K and Rb were released from primary minerals, possibly micas and feldspars in felsic rocks, during continental chemical weathering. Another possibility is that the increased CIA in the E2 interval

might have reflected a change in dust provenance associated with a shift in regional precipitation pattern. If a precipitation decreased in a previously wet (i.e., intensively weathered) region, the region could become a new source of high CIA dust to the Sakahogi section. However, if that was the case, the direction and intensity of prevailing winds, or the atmospheric circulation pattern, could have also changed, as well as the changes in dust provenance and hydrological cycle. Thus, this scenario should be carefully evaluated by further investigations for other marine and terrestrial records of the corresponding period.

The low-latitude zone of western Pangea might have been the major source of detrital elements to the deep-sea sediments of the equatorial Panthalassa (Nakada et al. 2014; Ikeda et al. 2015). Sedimentological studies in this region (e.g., the Petrified Forest National Park in Arizona) suggest an arid to semi-arid climate with significant seasonality during the Norian (Prochnow et al. 2006; Cleveland et al. 2007). However, the mean annual precipitation (MAP) inferred from a geochemical weathering index (the chemical index of alteration minus potassium index; Nordt et al. 2015) from the Chinle Formation in the Petrified Forest National Park (Fig. 2) suggests that short-term wetter periods could have occurred in the middle Norian (218–213 Ma; Ramezani et al. 2011; Ramezani et al. 2014). According to the age model of Nordt et al. (2015), these middle Norian climate shifts occurred close to the time of formation of the Manicouagan impact crater at 215.5 Ma (Jaret et al. 2018). A palynological record from the Chinle Formation (Baranyi et al. 2017) also demonstrated that gradual aridification during the Norian was interrupted by at least two short-lived wetter climatic periods in the middle Norian, as inferred from an increase in hygrophite vegetation. Given that the timing of this vegetation change in a wetter climatic period is very close to the age range of the Manicouagan impact event, Baranyi et al. (2017) suggested that the impact might have contributed to the vegetation change.

These studies have shown that the Manicouagan impact event might have coincided with middle Norian climate and vegetation changes during a short-lived wet period, which is consistent with our results showing intensified chemical weathering of the hinterland for ~300 kyr after the impact event. However, in the case of the Chicxulub impact event at the Cretaceous–Paleogene boundary, the environmental effects of climatically active gases (e.g., sulfur (di)oxide and carbon dioxide) released from the impact site were short-lived (years to hundreds of years; Artemieva et al. 2017), and cannot explain such a relatively long-term (~300 kyr) duration of intensified chemical weathering. The existing data imply no direct

causality between the Manicouagan impact event and the change to a wetter climate. However, the change to a warm, humid climate is an important factor in considering the controls on radiolarian burial flux, which will be discussed in the following section.

5.4 Decline of radiolarian burial flux

The E1 event is considered to have lasted 10^4 – 10^5 years after the impact event, based on Os isotope studies (Sato et al. 2013; Onoue et al. 2016a). Our geochemical data demonstrate that this interval represents the duration required for the restoration of burial flux by primary and silica- and apatite-secreting organisms after the middle Norian impact. A decline in radiolarian and conodont burial flux during the E1 event might be explained by the post-impact shutdown of primary productivity as discussed above. Our data also reveal that primary productivity and conodont burial flux had recovered to pre-impact values by the beginning of the E2 event. However, radiolarian burial flux did not recover until the E2 event, which was ~ 300 kyr after the impact (Onoue et al. 2016a). The mass accumulation rates (MAR) of radiolarian silica decreased from 0.1 to 0.02 g cm⁻² kyr⁻¹ across the impact and continued to decrease during the E2 interval (Fig. 3a).

Previous studies have suggested that radiolarian abundance is mainly controlled by the availability of dissolved silica and variations of temperature in the surface water (Anderson et al. 1989; Abelman and Gowing 1996; Boltovskoy et al. 2010; De Wever et al. 2014). Recently, Ikeda et al. (2017) suggested that the burial flux of biogenic silica (BSi) over a time scale longer than the residence time of dissolved silica in the ocean (generally < 100 kyr for the Phanerozoic) can be proportional to the silica input flux to the ocean that is controlled by global continental silicate weathering flux. Thus, the decline of radiolarian burial flux for ~ 300 kyr after the impact might be explained by suppressed continental silicate weathering. However, this is inconsistent with the inferred climatic changes toward a wetter condition and enhanced weathering in Pangea discussed above. In addition, MAR of radiolarian silica during the E2 event was an order of magnitude lower than the calculated BSi burial flux for the middle Norian (Ikeda et al. 2017). This discrepancy also suggests a fundamental gap between our observation and a simple mass balance model of oceanic dissolved silica during the E2 event, though we need further investigation to confirm the temporal variations in the radiolarian burial flux with a reliable sedimentation rate for the middle Norian chert. Changes in dissolved silica concentrations are also not sufficient to explain the decline of radiolarian silica burial flux during the E1 and E2 events, because silica-saturated conditions (≥ 110 mg/L SiO₂) with respect to biogenic

silica presumably existed in the Late Triassic (Racki and Cordey 2000; Grenne and Slack 2003). Furthermore, Si_{EF} during the E2 event is comparable to that in the other intervals before and after the impact, implying no significant change in the availability of silica in the studied section (Fig. 7). The $\delta^{13}\text{C}_{\text{org}}$ data suggest there was a resurgence in primary productivity after the E1 event (Fig. 3a, Onoue et al., 2016a). However, the recovery of radiolarian burial flux was significantly delayed (Fig. 3a). Taking these into consideration, other factors such as sea surface temperature must be invoked to account for the sustained reduction in the burial flux of radiolarian silica.

Relatively little information is available regarding the effects of seawater temperature variations on living radiolarians (Anderson et al. 1989; Anderson et al. 1990; Matsuoka and Anderson 1992). Experimental and observational studies have shown that the mean longevity and growth rate decrease markedly when temperature is raised. For example, laboratory culturing data for three tropical and subtropical radiolarian taxa (*Spongaster tetras*, *Didymocyrtis tetrathalamus*, and *Dictyornyne truncatum*) suggest that the maximum growth and longevity (mean longevity of 22–23 days) are achieved at a temperate condition of 21–28 °C, but skeletal growth and survival were remarkably suppressed at temperatures above 32 °C (longevity of 2 days), and no individuals survived at temperatures above 36 °C (Anderson et al. 1989; Anderson et al. 1990; Matsuoka and Anderson 1992). Furthermore, kinetic studies have shown that an increased temperature is the major factor that affects silica dissolution rates in the ocean (Erez et al. 1982; Ragueneau et al. 2000), which might enhance the in situ dissolution of radiolarian opal in surface waters.

Even if Norian radiolarians had different temperature tolerances, the consequences of climate warming would have affected the production of radiolarian opal in the near-surface waters. Our weathering proxy data (K_{EF}, Rb_{EF}, and CIA values) suggest acceleration of the hydrological cycle and an increase in continental chemical weathering rates, which is consistent with a greenhouse climate (e.g., Knobbe and Schaller 2018). Thus, we interpret that radiolarian silica burial flux did not recover until the E2 event due to an increased sea surface temperature. This interpretation is speculative—the existing data are unable to prove direct causality between greenhouse climate and the impact event, and the sea surface temperatures during the E1 and E2 events have yet to be determined by conodont $\delta^{18}\text{O}_{\text{apatite}}$ data (e.g., Rigo and Joachimski 2010; Rigo et al. 2012; Trotter et al. 2015; Knobbe and Schaller 2018). Furthermore, relationships to other environmental factors related to biogenic opal production, such as dissolved Al concentrations and microbial degradation of organic

matter (e.g., Van Bennekom et al. 1988; Nelson et al. 1995; Bidle and Azam 1999; Ragueneau et al. 2000), must be considered.

6 Conclusions

Stratigraphic profiles of major, trace, and rare earth elements in middle to upper Norian (Late Triassic) bedded cherts of the Mino Belt, central Japan, were constructed in order to assess the environmental changes that triggered a decline in radiolarian burial flux in the Panthalassa Ocean after the Norian impact event. Based on our geochemical data, paleoenvironmental changes across the Norian impact event can be summarized as follows.

1. Productivity and burial flux estimates based on $\delta^{13}\text{C}_{\text{org}}$ values and enrichments of Ba, Ca, P, and REEs suggest that there was a post-impact shut-down of productivity by primary and silica- and apatite-secreting organisms. Primary productivity and biogenic apatite (i.e., conodont) burial flux had recovered to pre-impact levels 10^4 – 10^5 years after the impact event, but radiolarian burial flux did not recover for ~ 300 kyr after the impact.
2. Redox-sensitive elements (Mn, V, U, and Mo) and Ce/Ce* anomalies exhibit limited fluctuations throughout the studied section, which indicate that there was no significant redox change in the pelagic realm of the Panthalassa Ocean across the Late Triassic impact event. Therefore, the change in redox conditions was not related to the decrease in radiolarian burial flux after the impact.
3. Weathering proxies, such as CIA values and enrichments of K and Rb, suggest that intense chemical weathering of the hinterland occurred during the decline in radiolarian burial flux after the Norian impact event. A short-lived wet period near the time of the Norian impact has been documented from the low-latitude zone of the western Pangean region (e.g., the Petrified Forest National Park in Arizona), which might have been the major source of detrital elements in the studied section. These data appear to reflect acceleration of the hydrological cycle and an increase in continental chemical weathering rates, which might have been induced by a greenhouse climate after the impact.
4. Radiolarian burial flux did not recover for ~ 300 kyr after the impact. We hypothesize that radiolarian burial flux decreased in response to an increased sea surface temperature due to a greenhouse climate, but this needs to be verified by independent data (e.g., conodont $\delta^{18}\text{O}_{\text{apatite}}$).

Abbreviations

PGE: Platinum group element; UCC: Upper continental crust; REE: Rare earth element; LREE: Light rare earth element; MREE: Middle rare earth element; HREE: Heavy rare earth element; CIA: Chemical Index of Alteration; MAP: Mean annual precipitation; MAR: Mass accumulation rates

Acknowledgements

We are grateful to Y. Itabashi and C. Kabashima for their assistance with sample preparation and chemical analyses at the University of Tokyo. K. Soda and D. Yamashita assisted with fieldwork and sample collection. Y. Isozaki, an anonymous reviewer and the editor, H. Kawahata are also thanked for their careful constructive reviews and editorial handling.

Authors' contributions

HS, KY, TO, and YK designed this study. HS, YT, KY, KF, and TO performed the geochemical analyses. All authors participated in the discussions to interpret the analytical results and aided in the writing of the manuscript. All authors read and approved the final manuscript.

Funding

This work was supported by the Japan Society for the Promotion of Science, Grant Numbers 15J30004 and 17K14409 to HS, 17H02975 to TO, and 15H05771 to YK.

Availability of data and materials

Please contact the corresponding author regarding data requests.

Competing interests

The authors declare that they have no competing interest.

Author details

¹Ocean Resources Research Center for Next Generation, Chiba Institute of Technology, 2-17-1 Tsudanuma, Narashino, Chiba 275-0016, Japan. ²Submarine Resources Research Center, Research Institute for Marine Resources Utilization, Japan Agency for Marine-Earth Science and Technology, 2-15 Natsushima-cho, Yokosuka, Kanagawa 237-0061, Japan. ³Faculty of Science and Engineering, Waseda University, 3-4-1 Okubo, Shinjuku-ku, Tokyo 169-8555, Japan. ⁴Frontier Research Center for Energy and Resources, School of Engineering, The University of Tokyo, 7-3-1 Hongo, Bunkyo-ku, Tokyo 113-8656, Japan. ⁵Department of Systems Innovation, School of Engineering, The University of Tokyo, 7-3-1 Hongo, Bunkyo-ku, Tokyo 113-8656, Japan. ⁶Department of Earth and Planetary Sciences, Kyushu University, 744 Motoooka, Nishi-ku, Fukuoka 819-0395, Japan.

Received: 5 February 2020 Accepted: 4 September 2020

Published online: 07 October 2020

References

- Abelmann A, Gowing MM (1996) Horizontal and vertical distribution pattern of living radiolarians along a transect from the Southern Ocean to the South Atlantic subtropical region. *Deep-Sea Res Part I* 43:361–382. [https://doi.org/10.1016/0967-0637\(96\)00003-9](https://doi.org/10.1016/0967-0637(96)00003-9)
- Algeo TJ, Ingall E (2007) Sedimentary C_{org} :P ratios, paleocean ventilation, and Phanerozoic atmospheric pO_2 . *Palaeogeogr Palaeoclimatol Palaeoecol* 256:130–155. <https://doi.org/10.1016/j.palaeo.2007.02.029>
- Algeo TJ, Kuwahara K, Sano H, Bates S, Lyons T, Elswick E, Hinnov L, Ellwood B, Moser J, Maynard JB (2011) Spatial variation in sediment fluxes, redox conditions, and productivity in the Permian–Triassic Panthalassic Ocean. *Palaeogeogr Palaeoclimatol Palaeoecol* 308:65–83. <https://doi.org/10.1016/j.palaeo.2010.07.007>
- Algeo TJ, Maynard JB (2004) Trace-element behavior and redox facies in core shales of Upper Pennsylvanian Kansas-type cyclothems. *Chem Geol* 206:289–318. <https://doi.org/10.1016/j.chemgeo.2003.12.009>
- Algeo TJ, Tribouillard N (2009) Environmental analysis of paleoceanographic systems based on molybdenum–uranium covariation. *Chem Geol* 268:211–225. <https://doi.org/10.1016/j.chemgeo.2009.09.001>
- Anderson OR, Bennett P, Bryan M (1989) Experimental and observational studies of radiolarian physiological ecology: 3. Effects of temperature, salinity and light intensity on the growth and survival of spongester tetras tetras maintained in laboratory culture. *Mar Micropaleontol* 14:275–282. [https://doi.org/10.1016/0377-8398\(89\)90014-5](https://doi.org/10.1016/0377-8398(89)90014-5)

- Anderson OR, Bryan M, Bennett P (1990) Experimental and observational studies of radiolarian physiological ecology: 4. Factors determining the distribution and survival of *Didymocystis tetrathalamus tetrathalamus* with implications for paleoecological interpretations. *Mar Micropaleontol* 16:155–167. [https://doi.org/10.1016/0377-8398\(90\)90001-3](https://doi.org/10.1016/0377-8398(90)90001-3)
- Ando A, Kodama K, Kojima S (2001) Low-latitude and Southern Hemisphere origin of Anisian (Triassic) bedded chert in the Inuyama area, Mino terrane, central Japan. *J Geophys Res Solid Earth* 106:1973–1986. <https://doi.org/10.1029/2000JB900305>
- Artemieva N, Morgan J, Expedition 364 Science Party (2017) Quantifying the release of climate-active gases by large meteorite impacts with a case study of Chicxulub. *Geophys Res Lett* 44:10180–10188. <https://doi.org/10.1002/2017GL074879>
- Baranyi V, Reichgelt T, Olsen PE, Parker WG, Kürschner WM (2017) Norian vegetation history and related environmental changes: New data from the Chinle Formation, Petrified Forest National Park (Arizona, SW USA). *Geol Soc Am Bull* 130:775–795. <https://doi.org/10.1130/B31673.1>
- Berndt J, Deutsch A, Schulte P, Mezger K (2011) The Chicxulub ejecta deposit at Demerara Rise (western Atlantic): dissecting the geochemical anomaly using laser ablation–mass spectrometry. *Geology* 39:279–282. <https://doi.org/10.1130/G31599.1>
- Bidle KD, Azam F (1999) Accelerated dissolution of diatom silica by marine bacterial assemblages. *Nature* 397:508–512. <https://doi.org/10.1038/17351>
- Bishop JKB (1988) The barite–opal–organic carbon association in oceanic particulate matter. *Nature* 332:341–343. <https://doi.org/10.1038/332341a0>
- Boltovskoy D, Kling SA, Takahashi K, Björklund KR (2010) World atlas of distribution of recent Polycystina (Radiolaria). *Palaeontol Electron* 13:1–229
- Breit GN, Wanty RB (1991) Vanadium accumulation in carbonaceous rocks: a review of geochemical controls during deposition and diagenesis. *Chem Geol* 91:83–97. [https://doi.org/10.1016/0009-2541\(91\)90083-4](https://doi.org/10.1016/0009-2541(91)90083-4)
- Calvert SE, Pedersen TF (1993) Geochemistry of recent oxic and anoxic marine sediments: implications for the geological record. *Mar Geol* 113:67–88. [https://doi.org/10.1016/0025-3227\(93\)90150-T](https://doi.org/10.1016/0025-3227(93)90150-T)
- Calvert SE, Pedersen TF (2007) Chapter fourteen elemental proxies for palaeoclimatic and palaeoceanographic variability in marine sediments: interpretation and application. In: Hillaire-Marcel C, Vernal AD (eds) *Developments in Marine Geology*, vol 1. Elsevier, pp 567–644. <https://www.sciencedirect.com/science/article/pii/S1572548007010196>
- Casacci M, Bertinelli A, Algeo TJ, Rigo M (2016) Carbonate-to-biosilica transition at the Norian–Rhaetian boundary controlled by rift-related subsidence in the western Tethyan Lagonegro Basin (southern Italy). *Palaeogeogr Palaeoclimatol Palaeoecol* 456:21–36. <https://doi.org/10.1016/j.palaeo.2016.05.007>
- Chen J, Algeo TJ, Zhao L, Chen Z-Q, Cao L, Zhang L, Li Y (2015) Diagenetic uptake of rare earth elements by bioapatite, with an example from Lower Triassic conodonts of South China. *Earth-Sci Rev* 149:181–202. <https://doi.org/10.1016/j.earscirev.2015.01.013>
- Cleveland DM, Atchley SC, Nordt LC (2007) Continental sequence stratigraphy of the Upper Triassic (Norian–Rhaetian) Chinle Strata, Northern New Mexico, U. S.A.: Alloctylic and Autocyclic Origins of Paleosol-Bearing Alluvial Successions. *J Sed Res* 77:909–924. <https://doi.org/10.2110/jsr.2007.082>
- Clutson MJ, Brown DE, Tanner LH (2018) Distal processes and effects of multiple Late Triassic terrestrial bolide impact: Insights from the Norian Manicouagan event, Northeastern Quebec, Canada. In: Tanner LH (ed) *Topics in Geobiology*, vol 46. Springer, pp 127–188. https://link.springer.com/chapter/10.1007/978-3-319-68009-5_5
- De Wever P, O'Dogherty L, Gorican S (2014) Monsoon as a cause of radiolarite in the Tethyan realm. *Compt Rend Geosci* 346:287–297. <https://doi.org/10.1016/j.crte.2014.10.001>
- Dehairs F, Chesselet R, Jedwab J (1980) Discrete suspended particles of barite and the barium cycle in the open ocean. *Earth Planet Sci Lett* 49:528–550. [https://doi.org/10.1016/0012-821X\(80\)90094-1](https://doi.org/10.1016/0012-821X(80)90094-1)
- Dymond J, Collier R (1996) Particulate barium fluxes and their relationships to biological productivity. *Deep Sea Research Part II: Top Stud Oceanogr* 43: 1283–1308. [https://doi.org/10.1016/0967-0645\(96\)00011-2](https://doi.org/10.1016/0967-0645(96)00011-2)
- Erez J, Takahashi K, Honjo S (1982) In-situ dissolution experiment of Radiolaria in the central North Pacific Ocean. *Earth Planet Sci Lett* 59:245–254. [https://doi.org/10.1016/0012-821X\(82\)90129-7](https://doi.org/10.1016/0012-821X(82)90129-7)
- Fujisaki W, Sawaki Y, Yamamoto S, Sato T, Nishizawa M, Windley BF, Maruyama S (2016) Tracking the redox history and nitrogen cycle in the pelagic Panthalassic deep ocean in the Middle Triassic to Early Jurassic: Insights from redox-sensitive elements and nitrogen isotopes. *Palaeogeogr Palaeoclimatol Palaeoecol* 449:397–420. <https://doi.org/10.1016/j.palaeo.2016.01.039>
- German CR, Elderfield H (1989) Rare earth elements in Saanich Inlet, British Columbia, a seasonally anoxic basin. *Geochim Cosmochim Acta* 53:2561–2571. [https://doi.org/10.1016/0016-7037\(89\)90128-2](https://doi.org/10.1016/0016-7037(89)90128-2)
- German CR, Elderfield H (1990) Application of the Ce anomaly as a paleoredox indicator: the ground rules. *Paleoceanogr* 5:823–833. <https://doi.org/10.1029/PA005i005p00823>
- Grenne T, Slack JF (2003) Paleozoic and Mesozoic silica-rich seawater: Evidence from hematitic chert (jasper) deposits. *Geology* 31:319–322 doi: 10.1130/0091-7613(2003)031<0319:PAMRSRS>2.0.CO;2
- Grygar TM, Mach K, Martinez M (2019) Checklist for the use of potassium concentrations in siliclastic sediments as paleoenvironmental archives. *Sed Geol* 382:75–84. <https://doi.org/10.1016/j.sedgeo.2019.01.010>
- Hollis CJ (2003) The Cretaceous/Tertiary boundary event in New Zealand: profiling mass extinction. *New Zealand J Geol Geophys* 46:307–321. <https://doi.org/10.1080/00288306.2003.9515011>
- Hollis CJ, Rodgers KA, Strong CP, Field BD, Rogers KM (2003) Paleoenvironmental changes across the Cretaceous/Tertiary boundary in the northern Clarence valley, southeastern Marlborough, New Zealand. *New Zealand J Geol Geophys* 46:209–234. <https://doi.org/10.1080/00288306.2003.9515005>
- Holser WT (1997) Evaluation of the application of rare-earth elements to paleoceanography. *Palaeogeogr Palaeoclimatol Palaeoecol* 132:309–323. [https://doi.org/10.1016/S0031-0182\(97\)00069-2](https://doi.org/10.1016/S0031-0182(97)00069-2)
- Hori RS, Cho CF, Umeda H (1993) Origin of cyclicity in Triassic–Jurassic radiolarian bedded cherts of the Mino accretionary complex from Japan. *The Island Arc* 2:170–180. <https://doi.org/10.1111/j.1440-1738.1993.tb00084.x>
- Hori RS, Fujiki T, Inoue E, Kimmura J-I (2007) Platinum group element anomalies and bioevents in the Triassic–Jurassic deep-sea sediments of Panthalassa. *Palaeogeogr Palaeoclimatol Palaeoecol* 244:391–406. <https://doi.org/10.1016/j.palaeo.2006.06.038>
- Hori RS, Higuchi Y, Fujiki T (2000) Chemical compositions and their environmental records of bedded cherts from accretionary complexes in Japan. *Memoir Geol Soc Jpn* 55:43–59
- Ikeda M, Hori RS, Okada Y, Nakada R (2015) Volcanism and deep-ocean acidification across the end-Triassic extinction event. *Palaeogeogr Palaeoclimatol Palaeoecol* 440:725–733. <https://doi.org/10.1016/j.palaeo.2015.09.046>
- Ikeda M, Tada R, Ozaki K (2017) Astronomical pacing of the global silica cycle recorded in Mesozoic bedded cherts. *Nat Commun* 8:15532. <https://doi.org/10.1038/ncomms15532>
- Imai N, Terashima S, Itoh S, Ando A (1995) 1994 compilation of analytical data for minor and trace elements in seventeen GSJ geochemical reference samples, "Igneous rock series". *Geostand Newslett* 19:135–213. <https://doi.org/10.1111/j.1751-908X.1995.tb00158.x>
- Isozaki Y (2014) Memories of Pre-Jurassic lost oceans: how to retrieve them from extant lands. *Geosci Canada* 41:283–311. <https://doi.org/10.12789/geocanj.2014.41.050>
- Jaret SJ, Hemming SR, Rasbury ET, Thompson LM, Glotch TD, Ramezani J, Spray JG (2018) Context matters – Ar–Ar results from in and around the Manicouagan Impact Structure, Canada: Implications for martian meteorite chronology. *Earth Planet Sci Lett* 501:78–89. <https://doi.org/10.1016/j.epsl.2018.08.016>
- Kamber BS, Webb GE (2001) The geochemistry of late Archaean microbial carbonate: implications for ocean chemistry and continental erosion history. *Geochim Cosmochim Acta* 65:2509–2525. [https://doi.org/10.1016/S0016-7037\(01\)00613-5](https://doi.org/10.1016/S0016-7037(01)00613-5)
- Kato Y, Fujinaga K, Suzuki K (2005) Major and trace element geochemistry and Os isotopic composition of metalliferous umbers from the Late Cretaceous Japanese accretionary complex. *Geochem Geophys Geosyst* 6. <https://doi.org/10.1029/2005GC000920>
- Kato Y, Fujinaga K, Suzuki K (2011) Marine Os isotopic fluctuations in the early Eocene greenhouse interval as recorded by metalliferous umbers from a Tertiary ophiolite in Japan. *Gond Res* 20:594–607. <https://doi.org/10.1016/j.gr.2010.12.007>
- Kato Y, Nakao K, Isozaki Y (2002) Geochemistry of Late Permian to Early Triassic pelagic cherts from southwest Japan: implications for an oceanic redox change. *Chem Geol* 182:15–34. [https://doi.org/10.1016/S0009-2541\(01\)00273-X](https://doi.org/10.1016/S0009-2541(01)00273-X)
- Kato Y, Ohta I, Tsunematsu T, Watanabe Y, Isozaki Y, Maruyama S, Imai N (1998) Rare earth element variations in mid-Archaean banded iron formations: Implications for the chemistry of ocean and continent and plate tectonics.

- Geochim Cosmochim Acta 62:3475–3497. [https://doi.org/10.1016/S0016-7037\(98\)00253-1](https://doi.org/10.1016/S0016-7037(98)00253-1)
- Kent DV, Olsen PE (2000) Magnetic polarity stratigraphy and paleolatitude of the Triassic–Jurassic Blomidon Formation in the Fundy Basin (Canada): implications for early Mesozoic tropical climate gradients. *Earth Planet Sci Lett* 179:311–324. [https://doi.org/10.1016/S0012-821X\(00\)00117-5](https://doi.org/10.1016/S0012-821X(00)00117-5)
- Knobbe TK, Schaller MF (2018) A tight coupling between atmospheric $p\text{CO}_2$ and sea-surface temperature in the Late Triassic. *Geology* 46:43–46. <https://doi.org/10.1130/G39405.1>
- Kutzbach JE, Gallimore RG (1989) Pangaeon climates: Megamonsoons of the megacontinent. *J Geophys Res Atmospheres* 94:3341–3357. <https://doi.org/10.1029/JD094iD03p03341>
- Liu D, Zhang C, Yang D, Pan Z, Kong X, Huang Z, Wang J, Song Y (2019) Petrography and geochemistry of the Lopingian (upper Permian)–Lower Triassic strata in the southern Junggar and Turpan basins, NW China: implications for weathering, provenance, and palaeogeography. *Int Geol Rev* 61:1016–1036. <https://doi.org/10.1080/00206814.2018.1490932>
- Lu Y, Makishima A, Nakamura E (2007) Coprecipitation of Ti, Mo, Sn and Sb with fluorides and application to determination of B, Ti, Zr, Nb, Mo, Sn, Sb, Hf and Ta by ICP-MS. *Chem Geol* 236:13–26. <https://doi.org/10.1016/j.chemgeo.2006.08.007>
- Makishima A, Nakamura E (2006) Determination of major, minor and trace elements in silicate samples by ICP-QMS and ICP-SFMS applying isotope dilution-internal standardisation (ID-IS) and multi-stage internal standardisation. *Geostand Geoanal Res* 30:245–271. <https://doi.org/10.1111/j.1751-908X.2006.tb01066.x>
- Matsuda T, Isozaki Y (1991) Well-documented travel history of Mesozoic pelagic chert in Japan: from remote ocean to subduction zone. *Tectonics* 10:475–499. <https://doi.org/10.1029/90TC02134>
- Matsuoka A, Anderson OR (1992) Experimental and observational studies of radiolarian physiological ecology: 5. Temperature and salinity tolerance of *Dictyocoryne truncatum*. *Mar Micropaleontol* 19:299–313. [https://doi.org/10.1016/0377-8398\(92\)90035-1](https://doi.org/10.1016/0377-8398(92)90035-1)
- McManus J, Berelson WM, Klinkhammer GP, Johnson KS, Coale KH, Anderson RF, Kumar N, Burdige DJ, Hammond DE, Brumsack HJ, McCorkle DC, Rushdi A (1998) Geochemistry of barium in marine sediments: implications for its use as a paleoproxy. *Geochim Cosmochim Acta* 62:3453–3473. [https://doi.org/10.1016/S0016-7037\(98\)00248-8](https://doi.org/10.1016/S0016-7037(98)00248-8)
- Murray RW (1994) Chemical criteria to identify the depositional environment of chert: general principles and applications. *Sed Geol* 90:213–232. [https://doi.org/10.1016/0037-0738\(94\)90039-6](https://doi.org/10.1016/0037-0738(94)90039-6)
- Murray RW, Buchholtz ten Brink MR, Gerlach DC, Price Russ III, Jones DL (1992) Interoceanic variation in the rare earth, major, and trace element depositional chemistry of chert: Perspectives gained from the DSDP and ODP record. *Geochim Cosmochim Acta* 56:1897–1913. [https://doi.org/10.1016/0016-7037\(92\)90319-E](https://doi.org/10.1016/0016-7037(92)90319-E)
- Murray RW, Leinen M (1993) Chemical transport to the seafloor of the equatorial Pacific Ocean across a latitudinal transect at 135°W: Tracking sedimentary major, trace, and rare earth element fluxes at the Equator and the Intertropical Convergence Zone. *Geochim Cosmochim Acta* 57:4141–4163. [https://doi.org/10.1016/0016-7037\(93\)90312-K](https://doi.org/10.1016/0016-7037(93)90312-K)
- Nakada R, Ogawa K, Suzuki N, Takahashi S, Takahashi Y (2014) Late Triassic compositional changes of aeolian dusts in the pelagic Panthalassa: Response to the continental climatic change. *Palaeogeogr Palaeoclimatol Palaeoecol* 393:61–75. <https://doi.org/10.1016/j.palaeo.2013.10.014>
- Nelson DM, Tréguer P, Brzezinski MA, Leynaert A, Quéguiner B (1995) Production and dissolution of biogenic silica in the ocean: Revised global estimates, comparison with regional data and relationship to biogenic sedimentation. *Glob Biogeochem Cycles* 9:359–372. <https://doi.org/10.1029/95GB01070>
- Nesbitt HW, Young GM (1982) Early Proterozoic climates and plate motions inferred from major element chemistry of lutites. *Nature* 299:715–717. <https://doi.org/10.1038/299715a0>
- Nordt L, Atchley S, Dworkin S (2015) Collapse of the Late Triassic megamonsoon in western equatorial Pangea, present-day American Southwest. *Geol Soc Am Bull* 127:1798–1815. <https://doi.org/10.1130/b31186.1>
- Nozaki T, Nikaido T, Onoue T, Takaya Y, Sato K, Kimura J-I, Chang Q, Yamashita D, Sato H, Suzuki K, Kato Y, Matsuoka A (2019) Triassic marine Os isotope record from a pelagic chert succession, Sakahogi section, Mino Belt, southwest Japan. *J Asian Earth Sci*: X 1:100004. <https://doi.org/10.1016/j.jaesx.2018.100004>
- Nürnberg CC, Bohrmann G, Schlüter M, Frank M (1997) Barium accumulation in the Atlantic sector of the Southern Ocean: Results From 190,000-year records. *Paleoceanogr* 12:594–603. <https://doi.org/10.1029/97PA01130>
- Ogg JG (2012) Triassic. In: Gradstein FM, Ogg JG, Schmitz MD, Ogg GM (eds) *The Geologic Time Scale 2012* vol 2. Elsevier, pp 681–730. <https://www.sciencedirect.com/science/article/pii/B9780444594259000251>
- Onoue T, Sato H, Nakamura T, Noguchi T, Hidaka Y, Shirai N, Ebihara M, Osawa T, Hatsukawa Y, Toh Y, Koizumi M, Harada H, Orchard MJ, Nedachi M (2012) Deep-sea record of impact apparently unrelated to mass extinction in the Late Triassic. *Proc Natl Acad Sci USA* 109:19134–19139. <https://doi.org/10.1073/pnas.1209486109>
- Onoue T, Sato H, Yamashita D, Ikehara M, Yasukawa K, Fujinaga K, Kato Y, Matsuoka A (2016a) Bolide impact triggered the Late Triassic extinction event in equatorial Panthalassa. *Sci Rep* 6:29609. <https://doi.org/10.1038/srep29609>
- Onoue T, Zonneveld J-P, Orchard MJ, Yamashita M, Yamashita K, Sato H, Kusaka S (2016b) Palaeoenvironmental changes across the Carnian/Norian boundary in the Black Bear Ridge section, British Columbia, Canada. *Palaeogeogr Palaeoclimatol Palaeoecol* 441:721–733. <https://doi.org/10.1016/j.palaeo.2015.10.008>
- Pfänder JA, Münker C, Stracke A, Mezger K (2007) Nb/Ta and Zr/Hf in ocean island basalts—Implications for crust-mantle differentiation and the fate of Niobium. *Earth Planet Sci Lett* 254:158–172. <https://doi.org/10.1016/j.epsl.2006.11.027>
- Plank T, Langmuir CH (1998) The chemical composition of subducting sediment and its consequences for the crust and mantle. *Chem Geol* 145:325–394. [https://doi.org/10.1016/S0009-2541\(97\)00150-2](https://doi.org/10.1016/S0009-2541(97)00150-2)
- Price JR, Velbel MA (2003) Chemical weathering indices applied to weathering profiles developed on heterogeneous felsic metamorphic parent rocks. *Chem Geol* 202:397–416. <https://doi.org/10.1016/j.chemgeo.2002.11.001>
- Prochnow SJ, Nordt LC, Atchley SC, Hudec MR (2006) Multi-proxy paleosol evidence for middle and late Triassic climate trends in eastern Utah. *Palaeogeogr Palaeoclimatol Palaeoecol* 232:53–72. <https://doi.org/10.1016/j.palaeo.2005.08.011>
- Racki G, Cordey F (2000) Radiolarian palaeoecology and radiolarites: is the present the key to the past? *Earth Sci Rev* 52:83–120. [https://doi.org/10.1016/S0012-8252\(00\)00024-6](https://doi.org/10.1016/S0012-8252(00)00024-6)
- Ragueneau O, Tréguer P, Leynaert A, Anderson RF, Brzezinski MA, DeMaster DJ, Dugdale RC, Dymond J, Fischer G, François R, Heinze C, Maier-Reimer E, Martin-Jézéquel V, Nelson DM, Quéguiner B (2000) A review of the Si cycle in the modern ocean: recent progress and missing gaps in the application of biogenic opal as a paleoproductivity proxy. *Glob Planet Change* 26:317–365. [https://doi.org/10.1016/S0921-8181\(00\)00052-7](https://doi.org/10.1016/S0921-8181(00)00052-7)
- Ramezani J, Fastovsky DE, Bowring SA (2014) Revised chronostratigraphy of the Lower Chinle Formation strata in Arizona and New Mexico (USA): High-precision U-Pb geochronological constraints on the Late Triassic evolution of dinosaurs. *Am J Sci* 314:981–1008. <https://doi.org/10.2475/06.2014.01>
- Ramezani J, Hoke GD, Fastovsky DE, Bowring SA, Therrien F, Dworkin SI, Atchley SC, Nordt LC (2011) High-precision U-Pb zircon geochronology of the Late Triassic Chinle Formation, Petrified Forest National Park (Arizona, USA): Temporal constraints on the early evolution of dinosaurs. *Geol Soc Am Bull* 123:2142–2159. <https://doi.org/10.1130/B30433.1>
- Reynard B, Lécuyer C, Grandjean P (1999) Crystal-chemical controls on rare-earth element concentrations in fossil biogenic apatites and implications for palaeoenvironmental reconstructions. *Chem Geol* 155:233–241. [https://doi.org/10.1016/S0009-2541\(98\)00169-7](https://doi.org/10.1016/S0009-2541(98)00169-7)
- Rigo M, Joachimski MM (2010) Palaeoecology of Late Triassic conodonts: Constraints from oxygen isotopes in biogenic apatite. *Acta Palaeontol Pol* 55: 471–478. <https://doi.org/10.4202/app.2009.0100>
- Rigo M, Trotter JA, Preto N, Williams IS (2012) Oxygen isotopic evidence for Late Triassic monsoonal upwelling in the northwestern Tethys. *Geology* 40:515–518. <https://doi.org/10.1130/G32792.1>
- Rudnick RL, Gao S (2014) Composition of the continental crust. In: Holland HD, Turekian KK (eds) *Treatise on Geochemistry*, vol 4, 2nd edn. Elsevier, Oxford, pp 1–51
- Sadiq M (1988) Thermodynamic solubility relationships of inorganic vanadium in the marine environment. *Mar Chem* 23:87–96. [https://doi.org/10.1016/0304-4203\(88\)90024-2](https://doi.org/10.1016/0304-4203(88)90024-2)
- Sato H, Onoue T, Nozaki T, Suzuki K (2013) Osmium isotope evidence for a large Late Triassic impact event. *Nat Commun* 4:2455. <https://doi.org/10.1038/ncomms3455>
- Sato H, Shirai N, Ebihara M, Onoue T, Kiyokawa S (2016) Sedimentary PGE signatures in the Late Triassic ejecta deposits from Japan: Implications for the

- identification of impactor. *Palaeogeogr Palaeoclimatol Palaeoecol* 442:36–47. <https://doi.org/10.1016/j.palaeo.2015.11.015>
- Schroeder JO, Murray RW, Leinen M, Pflaum RC, Janecek TR (1997) Barium in equatorial Pacific carbonate sediment: Terrigenous, oxide, and biogenic associations. *Paleoceanogr* 12:125–146. <https://doi.org/10.1029/96PA02736>
- Sephton MA, Amor K, Franchi IA, Wignall PB, Newton R, Zonneveld JP (2002) Carbon and nitrogen isotope disturbances and an end-Norian (Late Triassic) extinction event. *Geology* 30:1119–1122. [https://doi.org/10.1130/0091-7613\(2002\)0301119:CANIDA2.0.CO;2](https://doi.org/10.1130/0091-7613(2002)0301119:CANIDA2.0.CO;2)
- Sholkovitz ER, Landing WM, Lewis BL (1994) Ocean particle chemistry: the fractionation of rare earth elements between suspended particles and seawater. *Geochim Cosmochim Acta* 58:1567–1579. [https://doi.org/10.1016/0016-7037\(94\)90559-2](https://doi.org/10.1016/0016-7037(94)90559-2)
- Sholkovitz ER, Shaw TJ, Schneider DL (1992) The geochemistry of rare earth elements in the seasonally anoxic water column and porewaters of Chesapeake Bay. *Geochim Cosmochim Acta* 56:3389–3402. [https://doi.org/10.1016/0016-7037\(92\)90386-W](https://doi.org/10.1016/0016-7037(92)90386-W)
- Soda K, Onoue T (2019) Multivariate analysis of geochemical compositions of bedded chert during the Middle Triassic (Anisian) oceanic anoxic events in the Panthalassic Ocean. *Geochem J* 53:91–102. <https://doi.org/10.2343/geochemj.2.0540>
- Sugiyama K (1997) Triassic and Lower Jurassic radiolarian biostratigraphy in the siliceous claystone and bedded chert units of the southeastern Mino Terrane, Central Japan. *Bull Mizunami Fossil Mus* 24:79–193
- Tada R (1991) Compaction and cementation in siliceous rocks and their possible effect on bedding enhancement. In: Einsele G, Ricken W, Seilacher A (eds) *Cycles and Events in Stratigraphy*. Springer-Verlag, Berlin
- Takeo N (2005) Atlas of Eh-pH diagrams. Intercomparison of thermodynamic databases, Geological Survey of Japan Open File Report No.419
- Takiguchi T, Sugitani K, Yamamoto K, Suzuki K (2006) Biogeochemical signatures preserved in ancient siliceous sediments; new perspectives to Triassic radiolarian bedded chert compositions. *Geochem J* 40:33–45. <https://doi.org/10.2343/geochemj.40.33>
- Tanaka K, Watanabe N (2015) Size distribution of alkali elements in riverbed sediment and its relevance to fractionation of alkali elements during chemical weathering. *Chem Geol* 411:12–18. <https://doi.org/10.1016/j.chemgeo.2015.05.025>
- Taylor SR, McLennan SM (1985) *The continental crust: its composition and evolution*. Blackwell, Oxford
- Toyoda K, Tokonami M (1990) Diffusion of rare-earth elements in fish teeth from deep-sea sediments. *Nature* 345:607–609. <https://doi.org/10.1038/345607a0>
- Tribouillard N, Algeo TJ, Lyons T, Riboulleau A (2006) Trace metals as paleoredox and paleoproductivity proxies: An update. *Chem Geol* 232:12–32. <https://doi.org/10.1016/j.chemgeo.2006.02.012>
- Trotter JA, Williams IS, Nicora A, Mazza M, Rigo M (2015) Long-term cycles of Triassic climate change: a new $\delta^{18}\text{O}$ record from conodont apatite. *Earth Planet Sci Lett* 415:165–174. <https://doi.org/10.1016/j.epsl.2015.01.038>
- Uno K, Yamashita D, Onoue T, Uehara D (2015) Paleomagnetism of Triassic bedded chert from Japan for determining the age of an impact ejecta layer deposited on peri-equatorial latitudes of the paleo-Pacific Ocean: a preliminary analysis. *Phys Earth Planet Int* 249:59–67. <https://doi.org/10.1016/j.pepi.2015.10.004>
- Van Bennekom AJ, Berger GW, Van der Gaast SJ, de Vries RTP (1988) Primary productivity and the silica cycle in the Southern Ocean (Atlantic sector). *Palaeogeogr Palaeoclimatol Palaeoecol* 67:19–30. [https://doi.org/10.1016/0031-0182\(88\)90120-4](https://doi.org/10.1016/0031-0182(88)90120-4)
- Wanty RB, Goldhaber MB (1992) Thermodynamics and kinetics of reactions involving vanadium in natural systems: Accumulation of vanadium in sedimentary rocks. *Geochim Cosmochim Acta* 56:1471–1483. [https://doi.org/10.1016/0016-7037\(92\)90217-7](https://doi.org/10.1016/0016-7037(92)90217-7)
- Wignall PB, Zonneveld JP, Newton RJ, Amor K, Sephton MA, Hartley S (2007) The end Triassic mass extinction record of Williston Lake, British Columbia. *Palaeogeogr Palaeoclimatol Palaeoecol* 253:385–406. <https://doi.org/10.1016/j.palaeo.2007.06.020>
- Yamashita D, Kato H, Onoue T, Suzuki N (2018) Integrated Upper Triassic Conodont and Radiolarian Biostratigraphies of the Panthalassa Ocean. *Paleontol Res* 22:167–197. <https://doi.org/10.2517/2017PR020>
- Yao A, Matsuda T, Isozaki Y (1980) Triassic and Jurassic radiolarians from the Inuyama area, central Japan. *J Geosci Osaka City Univ* 23:135–154

- Yasukawa K, Liu H, Fujinaga K, Machida S, Haraguchi S, Ishii T, Nakamura K, Kato Y (2014) Geochemistry and mineralogy of REY-rich mud in the eastern Indian Ocean. *J Asian Earth Sci* 93:25–36. <https://doi.org/10.1016/j.jseas.2014.07.005>
- Zachos JC, Arthur MA, Dean WE (1989) Geochemical evidence for suppression of pelagic marine productivity at the Cretaceous/Tertiary boundary. *Nature* 337: 61–64. <https://doi.org/10.1038/337061a0>

Publisher's Note

Springer Nature remains neutral with regard to jurisdictional claims in published maps and institutional affiliations.

Submit your manuscript to a SpringerOpen[®] journal and benefit from:

- Convenient online submission
- Rigorous peer review
- Open access: articles freely available online
- High visibility within the field
- Retaining the copyright to your article

Submit your next manuscript at ► [springeropen.com](https://www.springeropen.com)